Cryptic variations in abyssal peridotite compositions: Evidence for shallow-level melt infiltration in the oceanic lithosphere

J. M. Warren and N. Shimizu

December 13, 2009

Abstract

Ranges in clinopyroxene trace elements of 2-3 orders of magnitude occur over <2 cm distance in peridotite samples from the Atlantis II Fracture Zone on the Southwest Indian Ridge. This represents the smallest length-scale at which clinopyroxene trace element concentrations have been observed to vary in abyssal peridotites. Due to the absence of any accompanying veins or other macroscopic features of melt-rock interaction, these peridotites are interpreted as being the result of cryptic metasomatism by a low volume melt. The small length-scale of the variations, including porphyroclastic clinopyroxene grains of 2 mm diameter with an order of magnitude variation in light rare earth elements, precludes an ancient origin for these anomalies. Calculation of diffusive homogenization timescales suggests that for the trace element variations to be preserved, metasomatism occurred in the oceanic lithospheric mantle at 1000-1200°C and 10-20 km depth. This observation provides constraints for the on-axis thickness of the lithospheric mantle at an ultra-slow spreading ridge. Trace amounts of plagioclase are present in at least two of the metasomatized samples. Textural and trace element observations indicate that it formed following the trace element metasomatism, indicating that the mantle can be infiltrated multiple times by melt during the final stages of uplift at the ridge axis. The peridotites in this study are from two oceanic core complexes on the Atlantis II Fracture Zone. Our observations of multiple late-stage metasomatic events in the lithospheric mantle agree with current models and observations of melt intrusion into the mantle during oceanic core complex formation. These observations also indicate that heterogeneous lithospheric mantle can be created at ultra-slow spreading ridges.

Introduction

Melting, melt transport and melt extraction at mid-ocean ridges are complex processes. Adiabatically ascending basaltic melts beneath mid-ocean ridges are known to react with and crystallize in wall-rock mantle peridotites (*Kelemen et al.*, 1992; *Seyler et al.*, 2001; *Brunelli et al.*, 2006). For example, porous melt flow results in replacive dunite formation via the dissolution of pyroxene and precipitation of olivine (e.g., *Kelemen et al.*, 1995). Dunites have been observed from all ridge systems (*Constantin et al.*, 1995; *Dick and Natland*, 1996; *Ghose et al.*, 1996; *Dick et al.*, 2003, 2010) and in ophiolites such as Trinity, Internal Ligurides, Oman, Josephine and Bay of Islands (*Kelemen et al.*, 1992; *Hoogerduijn Strating et al.*, 1993; *Boudier and Nicolas*, 1995; *Kelemen and Dick*, 1995; *Suhr et al.*, 2003). In addition to dunites, melt migration results in a large variety of vein lithologies that crystallize over a range of depths in the mantle, as demonstrated by *Python and Ceuleneer* (2003) from a survey of veins in the Oman Ophiolite. Among abyssal ultramafic samples, the formation of websterites and olivine websterites by the crystallization of trapped melts at depth has been documented at the Mid-Atlantic (MAR) and Southwest Indian (SWIR) ridges (*Dick et al.*, 1984; *Fujii*, 1990; *Juteau et al.*, 1990; *Dantas et al.*, 2007; *Warren et al.*, 2009).

In addition to reactive dunite formation and melt crystallization, melt flow through the mantle results in more cryptic forms of melt-rock reaction, often referred to as metasomatism. Mantle metasomatism has received widespread attention in the orogenic, ophiolite and xenolith literature (e.g., *Menzies et al.*, 1987; *Bodinier et al.*, 1990; *Van der Wal and Bodinier*, 1996; *Le Roux et al.*, 2007; *Hanghøj et al.*, 2010). However, metasomatism in these types of peridotites often relates to processes in the sub-continental lithospheric mantle. In abyssal peridotites, metasomatism is a direct result of the processes at mid-ocean ridges that also result in the formation of oceanic crust.

Typically, abyssal peridotites have been treated as the depleted residues of mantle melting (e.g., *Johnson et al.*, 1990), but more recent observations have recognized the importance of metasomatism beneath ridges. *Seyler et al.* (2001, 2007) presented textural evidence for the crystallization of

clinopyroxene (Cpx), spinel and sulfide in peridotites due to incomplete melt extraction at ridges. Asthenospheric metasomatism by an enriched mantle component has been identified at the SWIR on the basis of orthopyroxene (Opx) mineral inclusions with unusual mineralogy and high incompatible element concentrations (*Seyler et al.*, 2004). From trace element modeling, *Brunelli et al.* (2006) argued for weak refertilization of the mantle by low degree, partially aggregated melts, based on elevations in peridotite Cpx incompatible element concentrations. At the Romanche Fracture Zone on the MAR, peridotites contain up to 16% plagioclase, indicating regional-scale melt-rock interaction in the mantle (*Seyler and Bonatti*, 1997; *Tartarotti et al.*, 2002). *Dick et al.* (2010) found evidence at Kane Megamullion on the MAR for at least two types of metasomatism, in the form of variable alumina depletion in pyroxene rims in some residual peridotites and small amounts of plagioclase in others. Hence, melt migration through the shallow upper mantle can result in a variety of products, the results of which are diverse and reflect the conditions under which they occur.

In this study, we present a detailed analysis of centimeter to sub-centimeter scale melt-mantle interaction in peridotites from the SWIR. Our results further document the types of melt-mantle reactions that occur at ridges and provide constraints on the length-scales and magnitudes of these reactions. Peridotites in this study are from an ultra-slow spreading environment (ridge full spreading rate <20 mm/yr), where conductive cooling results in the cessation of melting at depth and the formation of a thinner basaltic crust (e.g., *Bown and White*, 1994; *Dick et al.*, 2003; *Montési and Behn*, 2007). Conductive cooling should result in both less depleted residual mantle and a greater potential for diverse reactions between ascending melts and wall-rock peridotite. In contrast, peridotites from the fast spreading East Pacific Rise (EPR) are highly depleted by melting, except where late melt fractions have locally reacted with the surrounding peridotite (*Cannat et al.*, 1990; *Dick and Natland*, 1996; *Constantin*, 1999).

Peridotites in this study are from two locations on the eastern side of the Atlantis II Fracture Zone on the SWIR (Fig. 1): the inside-corner high at the northern ridge transform intersection

(RTI) and a fossil inside-corner high located at 12 Ma along the fracture zone, known as Atlantis Bank (*Dick et al.*, 1991; *Baines et al.*, 2003; *John et al.*, 2004; *Baines et al.*, 2009). The full spreading rate in this area is 14.1 mm/yr, but due to asymmetrical spreading, the half-spreading rate to the south is 8.7 mm/yr (*Hosford et al.*, 2003; *Baines et al.*, 2007). During the formation of Atlantis Bank, *Baines et al.* (2008) estimate both a faster full spreading rate of 15.7 km/yr and highly asymmetrical spreading that resulted in a half spreading rate to the south of 14.1 mm/yr. Both Atlantis Bank and the current RTI are oceanic core complexes, exposed sections of lower crust and upper mantle that are exhumed by low angle detachment faulting at the ridge axis (*Cann et al.*, 1997; *Tucholke et al.*, 1998).

Previous work on peridotites from the Atlantis II Fracture Zone by *Johnson and Dick* (1992) and *Coogan et al.* (2004) investigated temporal variations in melt productivity, based on spatial variations in peridotite composition along the entire fracture zone. Peridotite Cpx trace element concentrations were used as a measure of melt depletion. Overall, light rare earth elements (LREE) were found to vary by approximately an order of magnitude along the fracture zone. In this study, vein-free spinel peridotites from the fracture zone are found to have 2-3 orders of magnitude variation in Cpx trace element concentrations. The large variations in trace elements at the centimeter-scale are demonstrated to indicate late-stage melt-rock reaction at the ridge. The role of metasomatism in the context of oceanic core complex formation is then discussed.

Methods

We analyzed 14 peridotites from two dredges and 5 submersible dives from the Atlantis II Fracture Zone, as shown in Fig. 1 and Table 1. Peridotites were analyzed for mineral modes and major and trace element compositions, combined with thin section petrography. Data for some peridotites from dredge RC27-9-6 are from *Lee* (1997) and are indicated as such in the tables. Modal analyses, given in Table 2, were made by point counting a minimum of 1400 points on large (51x75 mm)

thin sections at 1 mm intervals. Alteration pseudomorphs of primary phases were included in the counts of primary mineral phases (olivine, orthopyroxene, clinopyroxene, and spinel).

Silicate and oxide major element compositions were measured on the Massachusetts Institute of Technology JEOL JXA-733 Superprobes using wavelength dispersive spectroscopy, a 15kV accelerating potential and a 10nA beam current. Peak counting times were either 20 s or 40 s, except Fe in pyroxenes, which was 60 s. Data were reduced using matrix corrections (*Bence and Albee*, 1968) with modifications (*Albee and Ray*, 1970). For pyroxenes, a defocussed beam spot size of 10 μm was used for $\sim$10 analyses per 100 μm traverse to obtain bulk grain analyses that incorporate the effects of exsolution lamellae (Tables 3 and 4). Olivine, spinel and plagioclase were analyzed using a focussed beam and averaging 6 analyses per grain (Tables 5, 6 and 7). Using the same electron microprobe and similar analytical procedures for basaltic glass, *Gaetani and Grove* (1998) used repeat analyses to estimate analytical reproducibility: elements at $>$10 wt% levels are reproducible within 2%, elements at $<$10 wt% levels are reproducible within 5% and elements at $<$1 wt% level are reproducible within 30%.

Abundances of Na, Ti, Cr, Sr, Y, Zr and REE (La, Ce, Nd, Sm, Eu, Dy, Er, Yb) in Cpx (Tables 8 and 9) and plagioclase (Table 10) were determined by secondary ion mass spectrometry using the Cameca IMS-3f at Woods Hole Oceanographic Institution, following the technique of *Johnson et al.* (1990). Samples were ionized using a primary beam of O^- with an accelerating voltage of -8.30 kV and a current of 6-7 nA. The beam was focused to a $\sim$10 μm spot diameter for REEs and a $\sim$4 μm spot for other trace elements, with the trace element analytical spot positioned adjacent to the REE analysis. The energy filtering technique of *Shimizu et al.* (1978) was used to suppress molecular ion interferences, with a high voltage offset of 60 V for REE and 90 V for other elements. Working curves relating secondary ion intensity to concentration were determined using Cpx from the standard KH1 (Kilbourne Hole peridotite; *Irving and Frey*, 1984) for REEs and basalt glass standard KL2G (Kilauea tholeiite; *Jochum et al.*, 2000) for other trace elements. Standards were typically measured two or more times per session and the average value of all

5

standard analyses per session was used to calculate session-specific working curves.

Data were collected in 5 count cycles with count times of 30 s for REE and 5-20 s for other trace elements. For REE, ^{30}Si was measured at the start and end of each analysis, with the time interpolated average used to calculate REE/Si ratios, for determination of concentrations from the working curves. For the other trace elements, ^{28}Si was measured during each cycle, with the average value after all cycles used to determine concentrations. Traditionally, within-cycle ratios of REE/Dy and TE/Si are used to account for temporal variability in peak intensities (e.g., *Johnson et al.*, 1990; *Johnson and Dick*, 1992). Due to random background noise that produced occasional extremely high counts (1-3 orders of magnitude above the number of counts from the other cycles), this ratio scheme was abandoned. However, the error introduced by temporal variability in peak intensity is insignificant compared to primary beam instability, which cannot be monitored on the IMS-3f.

Low count rates among REEs are best treated statistically by a Poisson distribution, with the standard deviation given by $\sqrt{\overline{x}}$, where $\overline{x}$ is the 5 cycle raw count average for an element. To remove the effects of the random background noise, any individual REE count greater than $3\sqrt{\overline{x}}$ away from the *median* count value was discarded. After recalculating $\overline{x}$, any count more than $2\sqrt{\overline{x}}$ from the *average* count value was discarded. For the other trace elements, which have higher count rates, any count greater than 2 standard deviations from the *median* count value was discarded. After a final re-averaging of counts, element ratios to Si were calculated and concentrations derived from working curves.

Trace element analyses in abyssal peridotites are difficult due to their low concentrations, particularly for REE. We assessed data quality from measurements of an independent standard, sample count statistics, sample duplicate analyses, and REE pattern shape. All data were checked for the smoothness of their REE patterns and analyses with irregular patterns that were not reproduced by repeat analysis were discarded. REEs measured in an independent standard, Cpx from KLB-1 (Kilbourne Hole lherzolite; *Takahashi*, 1986, with trace element data by E. Nakamura, per-

6

sonal communication), provide an estimate of analytical reproducibility. From 21 analyses over 15 months, KLB-1 Cpx had a reproducibility of 9%-17%, depending on the element (Table 8). Analytical error can also be estimated from the count statistics of each analysis and by comparison of duplicate analyses (Table 8). The average % error in concentration based on the counting error ranges from 0.2-21% (Table 8), with LREE having the largest errors. The error based on the average difference between 35 pairs of duplicate analyses is also given in Table 8, based on data in this study and our unpublished dataset. The average deviation among duplicate analyses of Cpx ranges from 7% to 37%. We conclude that the error among duplicate analyses of Cpx provides the best measure of REE error. A comparative study by *Hellebrand et al.* (2002) of analytical conditions between the WHOI IMS-3f and the Max-Planck-Institute for Chemistry, Mainz IMS-3f demonstrated reproducibility of REE patterns within analytical error. Overall, despite the large errors, the ion probe provides useful and interpretable data due to the orders of magnitude variation in trace element concentrations and the overall smoothness and reproducibility of REE patterns.

Results

Description of the peridotites

The peridotites in this study are classified into two groups on the basis of their REE concentrations: residual peridotites and cryptically metasomatized peridotites (Table 2). In hand specimen and thin section, all 14 peridotites look like "typical" abyssal peridotites, with either porphyroclastic or protogranular textures and variable degrees of alteration. None of the peridotites contain veins. The modal variation of the peridotites is shown in Fig. 4, with Cpx modes varying by 3-9%, within the range of previously published modes for Atlantis II peridotites(*Johnson and Dick*, 1992; *Kumagai et al.*, 2003; *Morishita et al.*, 2007). All of these observations suggest that the peridotites are the depleted residues of melt extraction and the REE concentrations in 10 of the samples agree

7

with this interpretation. As shown in Fig. 5, these 10 residual peridotites have depleted REE patterns and are within the range of previously measured Atlantis II Fracture Zone peridotites.

The remaining 4 peridotites in this study have a large range in trace element concentrations (6K-458-3, 6K-465-2, and RC27-9-6-5) or an enriched composition (6K-458-1), as shown in Fig. 6. On the basis of the trace element enrichment, these peridotites are classified as cryptically metasomatized. In 3 of the 4 peridotites, 1-3 orders of magnitude variation in trace element concentration occurs across <2 cm distance. Fig. 3c shows that in one Cpx porphyroclast, Ce concentrations vary from 0.1 ppm to 2 ppm over a distance of <2 mm.

In hand specimen and thin section, the cryptically metasomatized peridotites have no veins and look like the other peridotites. Among the cryptically metasomatized peridotites, 6K-465-2 and RC27-9-6-5 have <50% alteration, with all primary phases present. The two samples from dive 6K-458 are more altered, with >50% serpentinization and no olivine preserved in 6K-458-3. Fig. 2 shows the hand specimen for sample 6K-465-2, which has a modal composition similar to the other peridotites in this study (Fig. 4). This sample contains none of the talc and amphibole veins that are found in some peridotites and that are often interpreted as altered melt veins. The edges of 6K-465-2 are planar, which could be interpreted as the contact with a vein. However, there is no alteration halo at the edge of the sample, as is often found at vein contacts. In addition, sample RC27-9-6-5, which also has a large range in trace elements, is sub-angular in shape with no planar surfaces that would represent a likely vein contact. This sample does contain a ∼1 mm wide zone of recrystallized olivine which is close to the observed trace element enrichment. The role of melt-rock reaction in enhancing deformation in peridotites has been discussed elsewhere (e.g., *Dijkstra et al.*, 2002) and was not pursued further in this study, particularly as the fine-grained shear zone in RC27-9-6-5 does not contain Cpx.

Overall, in none of the 4 enriched samples in this study is the cryptic metasomatism interpreted as originating from veins or dikelets within the samples. However, as will be discussed below, the metasomatic enrichments must have originated from a nearby vein or network of veins. Among the

8

other samples in the dives and dredge that contain the metasomatized peridotites, there is evidence for the presence of melt. In addition to the two metasomatized peridotites in Dive 458, a further two peridotites and two oxide gabbros were recovered. Dive 465 recovered a mix of peridotite, serpentinite, olivine gabbro and diabase. Of particular note is sample 6K-465-3, a peridotite with at least two generations of gabbro veins of highly evolved compositions that include minerals such as apatite, rutile and ilmenite. In dredge RC27-9-6, only peridotite and dunite where recovered. However, one of the peridotites has a clinopyroxenite vein, discussed by *Warren et al.* (2009), and another sample contains a gabbro vein. Both the dives and the dredge sampled ∼1 km of seafloor and better spatial constraints for the relationship between samples within dives or dredges cannot be determined. In the dives, precise sample locations are available, but none of the samples where attached to outcrops and thus they originated at an unknown distance upslope of the sample location.

Trace elements

Plots of REEs in Cpx for each of the 10 residual abyssal peridotites are shown in Fig. 5. Cpx REE compositions are compared to the range of other Atlantis II Fracture Zone peridotite Cpx from *Johnson and Dick* (1992). In addition, Cpx is compared to the predicted composition of Cpx in the depleted MORB (mid-ocean ridge basalt) mantle (DMM, *Workman and Hart*, 2005). DMM is a hypothetical composition for the depleted upper mantle, derived from the average isotopic composition of MORB. All 10 peridotites have depleted patterns that are within the range of other Atlantis II Fracture Zone peridotite Cpx (*Johnson and Dick*, 1992).

The REE patterns for the 4 cryptically metasomatized peridotites are shown in Fig. 6. In 3 of the samples, trace elements vary spatially from depleted to enriched compositions, as indicated in Fig. 2. Grains located in the transition zone between the enriched and depleted portions of the peridotites have core to rim variations in concentration, as shown for a Cpx porphyroclast in Fig. 3c and plotted in Fig. 6. Note that the two dimensional slice of the Cpx grain in Fig. 3c may not

9

represent a true section through the grain core. As this grain is spatially located at the transition between enriched and depleted portions of the peridotite, this would only indicate that the trace element enrichment did not penetrate deep into the grain. In contrast, other porphyroclasts have similar core and rim concentrations (Table 8), with the entire grain being either enriched or depleted. In sample 6K-458-1, all analyzed Cpx are relatively enriched in REE, with concentrations similar to DMM, but with negative Eu anomalies. As this sample was collected near sample 6K-458-3, which contains both depleted and enriched grains, the enriched trace elements in 6K-458-1 may be related, a possibility that is discussed further below.

Texturally, Cpx in the metasomatized peridotites vary from porphyroclasts to recrystallized grains; the latter are found as aggregates or as elongate grains adjacent to Opx. However, Cpx textures do not correlate with trace elements, with porphyroclastic and interstitial grains having the same trace element concentrations, but varying spatially across the thin sections. Three Cpx porphyroclasts from 6K-465-2 that encompass the full range of trace element abundances, but are texturally identical, are shown in Fig. 3a-c. These grains are relatively coarse (1-3 mm), with smoothly curved grain boundaries containing some complex cusps and lobes. The absence of a textural correlation to the trace element abundance variations suggests that the trace element enrichment is unrelated to the melting which initially depleted the peridotite.

In two of the four cryptically metasomatized peridotites, the rims of both depleted and enriched Cpx have negative Eu anomalies, but the cores do not (Fig. 6). Trace amounts of plagioclase were identified in these samples, present as tiny grains adjacent to spinel and in clusters with olivine (Fig. 3d). The observation of Eu anomalies in rims but not cores of depleted and enriched Cpx suggest that plagioclase formation occurred after the melt-rock reaction event. The trace element concentrations in plagioclase around the spinel grain in Fig. 3d are highly variable, with Sr ranging from 1 to 58 ppm (Table 10).

10

Major elements

Mineral phases in the cryptically metasomatized peridotites have mantle major element compositions: olivine is Fo_{90}, Opx is Mg# 90 [$=Mg/(Mg+Fe)$] and Cpx is Mg# 91. Plots of Cpx Mg# against Cr# [$=Cr/(Cr+Al)$] and Na_2O in Fig. 7 demonstrate that the cryptically metasomatized peridotites have the same range in major element compositions as other Atlantis II residual peridotites. Some Cpx extend to high Cr# (=20), but residual Cpx also extend toward high Cr#.

Spinel compositions are plotted in Fig. 8. The variation of spinel Cr# and Mg# follows the general trend for depletion of peridotites during melting, with Cr# increasing during melting while Mg# decreases over a more limited range (*Dick and Bullen*, 1984). Spinels from Atlantis II tend to have low Cr# (typically <30) and high Mg# (typically >70), suggesting a limited degree of melting. In Fig. 8b, spinel TiO_2 is plotted as a function of Cr#. TiO_2 is incompatible in spinel, though its incompatibility may decrease with increasing Cr# (Hellebrand, personal communication). Most spinels that plot off the Cr# - Mg# trend also have high TiO_2, suggesting that these parameters combined indicate refertilization of the peridotite by differentiated melts.

In the cryptically metasomatized peridotites, spinels are irregularly shaped with deep embayments and generally <1 mm diameter, though some grains reach 5 mm length. Spinel Cr# varies from 15 to 49 and intra-sample variations in spinel Cr# are large (Table 6). Grains with high Cr# tend to have higher TiO_2, further indication that the cryptic metasomatism is the result of melt refertilization. Around some spinels, trace amounts of plagioclase are present as equant intergrowths with olivine around spinel. For example, in sample 6K-465-2, the highest Cr# spinel is a tiny grain that from textural relationships appears to have reacted with pyroxenes to form the low pressure assemblage of plagioclase and olivine (Fig. 3).

Discussion

Mechanisms of peridotite metasomatism

Mantle melting during adiabatic upwelling beneath mid-ocean ridges is near-fractional, meaning that upward extraction (migration) of melt from the site of melting should be efficient. As the mantle moves upward, continued melt formation and extraction occurs. Hence, residual peridotite becomes increasingly more depleted in incompatible elements, as observed in abyssal peridotite Cpx compositions (e.g., *Johnson et al.*, 1990; *Hellebrand et al.*, 2001; *Brunelli et al.*, 2006). At the grain scale, while melt mass is increasing, mantle melting proceeds with continual reaction among peridotite minerals and melt (*Liang*, 2003).

As melt migration is faster than the upward flow of residual peridotites, minerals in residual peridotites can come into contact with and react with percolating melts under disequilibrium conditions (e.g., *Kelemen et al.*, 1992; *Morgan et al.*, 2008). Reactions between melt and peridotite can occur regardless of whether melt flow is focused or not, and could take a variety of forms, including dissolution, crystal growth, or chemical exchange between crystals and melt without modal changes, depending on pressure, temperature, melt composition, and melt-rock ratio, among other variables. The observation of pyroxenite and gabbro veins in abyssal peridotites (e.g., *Dick*, 1989; *Dantas et al.*, 2007; *Warren et al.*, 2009) indicates that melts beneath mid-ocean ridges directly intrude into peridotite, along with forming the melt/rock reaction zones associated with dunites. These veins suggest that the crystallization of melts within the mantle is often an important process at mid-ocean ridges and that melt extraction is not always as efficient as suggested by near-fractional melting models.

The thermal regime of the Atlantis II Fracture Zone is controlled by the low spreading rate (14 mm/yr) and the fracture zone, which result in a limited degree of melting due to conductive cooling from above (*Bown and White*, 1994). Under these conditions, migrating melt is cooled and melt extraction is expected to be incomplete. In abyssal peridotites, evidence for incomplete

melt extraction at low and high melt/rock ratios over a range of pressures is recognized in the form of interstitial Cpx, spinel and/or plagioclase, and magmatic veins (*Dick*, 1989; *Cannat et al.*, 1992; *Constantin et al.*, 1995; *Seyler and Bonatti*, 1997; *Seyler et al.*, 2001; *Warren et al.*, 2009). Refertilization by low volume melts percolating along grain boundaries results in more cryptic forms of refertilization, the signature of which is difficult to detect. However, recent detailed studies − in particular by Seyler and co-workers − (*Seyler et al.*, 2001, 2004, 2007; *Hellebrand et al.*, 2002; *Brunelli et al.*, 2006) have documented that many residual peridotites have undergone low degrees of refertilization, with small enrichments in the most incompatible trace elements, the formation of interstitial Cpx veinlets and/or trace metasomatic phases (e.g., amphibole, apatite and mica). In addition, residual abyssal peridotites are not as LREE depleted as they should be if they have undergone only melt extraction (*Hellebrand et al.*, 2002; *Brunelli et al.*, 2006). Modeling by *Brunelli et al.* (2006) suggests that all depleted peridotites have been weakly refertilized by 0.1-1% instantaneous or partially aggregated melts trapped during melt percolation.

"Residual" peridotite Cpx in this study are strongly depleted in LREE (Fig. 5). Their trace element abundance patterns are consistent with residues of fractional melting (*Johnson et al.*, 1990), possibly followed by a low degree of refertilization (*Brunelli et al.*, 2006). Residual Cpx occur as porphyroclasts with 1-5 mm diameter and with exsolution lamellae. In general, their cores and rims are indistinguishable with respect to trace element abundances (Table 9). Various studies have attempted to constrain whether minerals remain in equilibrium with melt during mantle melting or whether diffusion limits equilibrium (*Qin*, 1992; *Iwamori*, 1992, 1993; *Van Orman et al.*, 2002; *Cherniak and Liang*, 2007). The lack of clear evidence for systematic incompatible element depletion of the rims of Cpx grains relative to cores indicates that Cpx and melt remained in equilibrium during melt extraction at the SWIR.

Cpx in residual peridotites also occur as interstitial grains of <1 mm size without exsolution lamellae. The elongate morphology of some interstitial grains suggests that they formed by crystallization of melt along grain boundaries, but the majority are more equant in shape, suggestive of

13

recrystallization during ductile flow in the asthenosphere. Table 9 shows that interstitial grains in residual peridotites have similar compositions to porphyroclast cores. This suggests that the melt from which elongate interstitial Cpx crystallized also re-equilibrated with the porphyroclastic Cpx.

"Metasomatic" Cpx in this study are those with large abundance variations or high concentrations of incompatible elements. Samples with metasomatic Cpx vary from LREE-depleted, residual-type patterns to LREE-enriched patterns over small (<2 cm) length-scales. These variations are taken as evidence of cryptic metasomatism by a percolating melt. The length-scales of the trace element variations are not large enough to be preserved for long times (e.g., >1 My) at mantle temperatures, as will be demonstrated below. As there is no evidence for rapid uplift or rapid cooling of the core complexes at the Atlantis II Fracture Zone (*John et al.*, 2004), the metasomatism must be related to shallow-level late-stage magmatic processes in oceanic core complexes; this will be discussed in the final section.

Descriptions and models of the interactions of peridotites with migrating melts and fluids have a long history in studies of mantle metasomatism of the continental lithosphere (e.g., *Menzies et al.*, 1987; *Bodinier and Godard*, 2003). *Navon and Stolper* (1987) and *Bodinier et al.* (1990) were among the first to attempt to explain melt-rock reaction in a quantitative fashion. These early models concentrated on explaining variations among peridotite Cpx trace element patterns and did not include the modal changes that occur during melt-rock reaction. More generalized models that include mineralogical reactions have since been developed (*Godard et al.*, 1995; *Vernières et al.*, 1997).

Particularly interesting and relevant to this study is the chromatographic fractionation of trace elements predicted by these models. As melt percolates around mantle minerals, fractionation of trace elements occurs because of the differences among mineral-melt partition coefficients for different elements. When an enriched small-degree melt enters a column of depleted peridotite, REE patterns of Cpx in the peridotite will be modified successively, beginning with an increase in the most incompatible LREE and progressing towards less incompatible HREE. This process can

14

result in Cpx with "spoon-shaped" and "sharply inflected" REE patterns, as observed by *Takazawa et al.* (1992) in depleted lherzolites from the Horoman peridotite massif and by *Sen et al.* (1993) in xenoliths from Oahu. In Fig. 6, REE in some Cpx from abyssal peridotite RC27-9-6-5 have inflected "spoon-shape" patterns.

Sample 6K-465-2 illustrates two salient features studied here: first, metasomatism occurs on small length-scales (Figs. 2 and 3), and second, the magnitude of metasomatic changes is extremely large for incompatible elements (Fig. 6). In particular, the transition from unmetasomatized residual Cpx to completely metasomatized Cpx occurs over a distance of <1 cm (Fig. 2). Zoned Cpx (Fig. 3b) only occur in the transition between depleted (unmetasomatized) and enriched (metasomatized) portions of the rock. These observations suggest that the trace element variations record the metasomatic front. The metasomatized Cpx in Fig. 6 have REE abundances that are compatible with LREE-enriched basalts from the Atlantis II Fracture Zone (*Johnson and Dick*, 1992), though they would be in equilibrium with melts with slightly higher REE concentrations than are observed.

Fig. 9 demonstrates the difference between melting and melt-rock reaction in the depleted versus the metasomatized peridotites. The variation of Zi and Ti in peridotite Cpx was used by *Johnson et al.* (1990) to estimate degree of melting, as Ti is less incompatible in Cpx than Zr. Depleted peridotites from Atlantis II Fracture Zone follow this general melting trend of decreasing Ti and Zr. In contrast, cryptically metasomatized Cpx do not plot on the fractional melting trend, but instead follow a trend with a shallower slope, indicating that the increase in Zr is greater than that in Ti during metasomatism. Since the Cpx/melt partition coefficient for Zr is smaller than that for Ti, this trend is interpreted as being consistent with the chromatographic effect. A similar observation was made by *Tartarotti et al.* (2002) for Cpx in plagioclase peridotites from the Romanche Fracture Zone. The most enriched Cpx from the Atlantis II peridotites plots close to the field of basalts from the fracture zone. However, Cpx from the metasomatized peridotites are not in equilibrium with the basalts, indicating that they did not form by direct precipitation from a

15

376 basaltic melt sampled at the fracture zone.

377 The cryptically metasomatized peridotites represent the smallest length-scale at which com-
378 positional variation has been observed in abyssal peridotites. The REE variations in the cryptic
379 peridotites are similar to the theoretical predictions of chromatographic melt-rock reaction mod-
380 els, for example by *Vernières et al.* (1997). However, given the small size of he samples and
381 the limited spatial information on the exact three dimensional shape of the zoning front, detailed
382 modeling is precluded at this point. Instead, diffusion calculations are used to place constraints
383 on the timing of cryptic metasomatism. Our diffusion analysis is similar to that employed by *Sen*
384 *et al.* (2003) for Hawaiian xenoliths, in which they observed small-scale variations in Cpx and
385 plagioclase trace elements.

386 To assess the time-scales for diffusive homogenization, the approximation $x = \sqrt{D_i t}$ is used,
387 where x is distance, D_i is the diffusion coefficient for an element i, and t is time. Diffusion coef-
388 ficients for Ce and Yb in Cpx were extrapolated from the *Van Orman et al.* (2001) experimental
389 dataset and for Sr from *Sneeringer et al.* (1984). The depth and pressure to a given isotherm be-
390 neath the ridge axis, listed in Table 11, were calculated using the scaling relations determined by
391 *Montési and Behn* (2007), which uses a finite element model to determine ridge thermal structure.
392 Diffusion coefficients in Table 11 were calculated over a temperature range of 700-1350°C. At a
393 given temperature, Sr is the fastest diffusing species in Cpx and Ce the slowest. Over the temper-
394 ature range of the calculation, the diffusion coefficient for each element varies by many orders of
395 magnitude. For example, at 1350°C, D_{Ce} is 4x10^{-20} m²/s, whereas at 700°C, D_{Ce} is 8x10^{-30} m²/s
396 (Table 11). Diffusion lengthscales have been calculated for Cpx grain radii of 1 mm, the smallest
397 lengthscale at which trace elements vary, and at 1 cm, the maximum lengthscale of variability.
398 While 1 cm is larger than the radii of Cpx in this study, it is taken as a proxy for diffusivity across
399 the 2 cm diameter zone over which trace element disequilibrium is observed.

400 The results of the diffusion calculation are plotted in Fig. 10, which shows the time for diffusive
401 equilibration as a function of temperature for grains of 1 mm and 1 cm radii. The upwelling time

16

from the depth of a given isotherm to the seafloor is also shown in Fig. 10, calculated from the ridge corner flow equation (Table 11). This line separates grain sizes and temperatures where diffusive equilibration of the peridotite can occur within the timescale of mid ocean ridge upwelling, from those where diffusion is too slow for homogenization. For example, at 700°C and 6 km depth, diffusive equilibration does not occur at either the millimeter or centimeter lengthscales (assuming that extrapolation of the diffusion data to this temperature is valid). In contrast, at 1350°C and 37 km depth, trace element gradients in Cpx at the millimeter to centimeter length scales will diffusively homogenize in 7 My. Even though Cpx will also cool during those 7 My, slowing diffusion, the calculation indicates that ~1 My is sufficient time for diffusive homogenization of all elements. Hence, the variations observed in samples such as 6K-465-2 can not be preserved if they form at 1350°C, indicating that the metasomatism occurred after the peridotite had cooled below its solidus and adiabatic decompression melting had stopped.

The first order diffusion calculation can be used to place further constraints on the pressure and temperature of the peridotite metasomatism. The variability of trace element concentrations between the enriched and depleted portions of the peridotite vary depending on the element, with the more incompatible elements showing larger variability. For example, the average concentration of Ce in the depleted region of sample 6K-465-2 is 0.08 ± 0.09 ppm, whereas in the enriched region it has an average concentration two orders of magnitude higher, 3.46 ± 2.48 ppm. Yb shows less variability, with an average of 1.22 ± 0.31 ppm in the depleted region and 2.69 ± 1.34 ppm in the enriched region. Finally, Sr is relatively homogeneous in the sample, with an average composition in the depleted region of 2.10 ± 1.54 ppm and in the enriched region of 1.64 ± 0.68 ppm. Comparing these observations to Fig. 10, this pattern is best matched if the metasomatism occurred around 1100°C and 14 km depth.

Two of the metasomatized peridotites are from Atlantis Bank on the Atlantis II Fracture Zone. *Baines et al.* (2008) estimate that during formation of Atlantis Bank at 12 Ma, the full ridge spreading rate was faster and more asymmetrical, with a half spreading rate to the south of 14.1 mm/yr.

This analysis is based on analysis of both magnetic isochrons and Pb/U dating of magmatic zircons from Atlantis Bank gabbros. This faster spreading rate indicates faster upwelling and thus less time for diffusive equilbiration. Calculating diffusion length scales to match the pressure-temperature profile for this faster spreading rate indicates that for diffusive homogenization of Sr to occur, the metasomatism must have occurred around 1200°C and 10 km depth.

Overall, the trace element data for the 4 metasomatized peridotites suggest that metasomatism of this type occurs at temperatures of ∼1000-1200°C and depths of ∼10-20 km. This implies shallow, late-stage melt infiltration of the lithospheric mantle at the ridge axis, which has cooled below its solidus. Hence, this provides a direct observation that the lithosphere at the ridge axis can have a finite thickness of 10-20 km, unlike standard ridge models where adiabatically upwelling asthenospheric mantle extends (theoretically) to the crust (e.g., *Klein and Langmuir*, 1987; *McKenzie and Bickle*, 1988; *Kinzler and Grove*, 1992).

Formation of plagioclase in the metasomatized peridotites

Plagioclase is present in trace quantities (<0.01%) in at least two of the four cryptically metasomatized abyssal peridotites. Plagioclase grains are <1 mm diameter and found in association with spinel. Plagioclase may be present in the other two metasomatized peridotites, especially as Cpx in 6K-458-1 have negative Eu anomalies. However, plagioclase is difficult to identify at the trace level, particularly in more altered samples such as 6K-458-1 and 6K-458-3. Plagioclase has not been been found in the 10 depleted peridotites in this study, though Cpx in some of the samples have small negative Eu anomalies, suggesting that plagioclase may be present.

Technically all abyssal peridotites should contain plagioclase, not spinel, as Al-spinel is metastable at shallow depths in the mantle. Around a depth of ∼20-30 km, the high-pressure mineral assemblage should breakdown via the reaction (*Green and Hibberson*, 1970; *Borghini et al.*, 2010): Al-Spinel + Clinopyroxene + Orthopyroxene → Plagioclase + Olivine + Cr-Spinel. However, depleted abyssal peridotites are all spinel peridotites. Trace (<0.1%) plagioclase has been identified

18

in only 15% of abyssal peridotites, based on a literature compilation of modal data for 493 depleted abyssal peridotites. The metastability of spinel is partly due to Cr, as Cr-spinel extends the spinel stability field to ~15 km (*Asimow et al.*, 1995). However, the general lack of plagioclase in depleted abyssal peridotites suggests that there is a kinetic barrier to spinel breakdown.

An alternative explanation for the presence of plagioclase is crystallization from an infiltrating melt. Plagioclase formed by melt impregnation has been documented in abyssal, ophiolitic, orogenic and xenolith peridotites (e.g., *Dick*, 1989; *Seyler and Bonatti*, 1997; *Dijkstra et al.*, 2001; *Sen et al.*, 2003; *Müntener and Piccardo*, 2003; *Borghini et al.*, 2007; *Kaczmarek and Müntener*, 2008). However, in these examples the amount of plagioclase in peridotites is generally >1% and can approach 20%. Grains often occur as large porphyroclasts, not just small interstitial grains. In contrast, plagioclase in the metasomatized peridotites in this study are interstitial grains associated with interstitial olivine at the embayed edges of spinel (Fig. 3d).

Two characteristics of plagioclase in the metasomatized peridotites indicate that they are not the result of the melt infiltration events that produced large trace element variations. The first is that plagioclase is found in the depleted, not the enriched, regions of the peridotites (Fig. 2). The second is the pattern of negative Eu anomalies in Cpx that occur when plagioclase is present. These anomalies are due to the preferential partitioning of Eu^{2+} into plagioclase, the only REE that occurs in both +2 and +3 valence states. The cores of both enriched and depleted Cpx generally have no Eu anomaly, whereas the rims of both types of Cpx have negative anomalies. The occurrence of Eu anomalies in Cpx rims but not cores is shown in Fig. 11, by the ratio of Eu* (the predicted Eu concentration calculated from Sm and Dy concentrations) to measured Eu concentration. In the REE patterns in Fig. 5, most Cpx cores in 6K-465-2 and RC27-9-6-5 are observed to have no negative Eu anomaly. Note, however, that in the plot of 6K-465-2, some cores have negative anomalies, which is probably due to the thin section being cut through the rim of these Cpx.

The lack of an Eu anomaly in enriched and depleted Cpx cores, and the presence of a negative anomaly in all Cpx rims, indicates that plagioclase formation occurred after the metasomatism. If

plagioclase crystallized during the metasomatic event, then the REE patterns of enriched Cpx cores should have negative Eu anomalies. In contrast, Cpx rims from depleted and enriched regions of the peridotite have negative Eu anomalies (Fig. 11). Rim depletion in Eu could have occurred if plagioclase formed by spinel breakdown or if it formed by crystallization from a later, low-volume infiltrating melt.

Sr also preferentially partitions into plagioclase, however Sr concentrations are similar in Cpx cores and rims, and in the enriched and depleted regions of the peridotite. This is probably due to diffusive homogenization, assuming that Sr is faster diffusing than Eu. Though no diffusion data for Eu in Cpx exists, the diffusion coefficient of Eu^{3+} in Cpx can be assumed to be within the REE range (*Van Orman et al.*, 2001) . It is also unclear whether Sr has a negative or positive anomaly in the metasomatized peridotites. If the traditional ordering of trace elements is used, then Sr plots as a negative anomaly between Nd and Sm. However, this element order is based on the partitioning of elements into basaltic melt (*Hofmann*, 1988). Consideration of plagioclase-Cpx partitioning for Sr suggests that in both minerals Sr is more incompatible than La, due to its larger ionic radius. Using this ordering of the elements, depleted regions of the peridotites have positive Sr anomalies (with respect to La) and enriched regions have negative Sr anomalies. These apparent anomalies are due to variation in La concentrations, as the average Cpx Sr concentration does not vary between the depleted (2.56 ± 1.56 ppm) and enriched (2.65 ± 1.75 ppm) regions of the peridotites. As discussed in the previous section, the lack of Sr variability suggests that Sr has diffusively equilibrated across the metasomatized peridotites. Plagioclase formation can then be considered to have lowered the Sr concentration of both Cpx cores and rims, due to faster diffusion and a Sr Plag/Cpx partition coefficient that is larger for Sr ($\sim$9) than for Eu ($\sim$2), estimated from *Wood and Blundy* (2003).

Plagioclase with a breakdown origin in abyssal peridotites has rarely been identified. In most examples of plagioclase abyssal peridotites, high modal proportions of plagioclase and relatively fertile compositions indicate a melt origin (e.g., *Dick*, 1989; *Seyler and Bonatti*, 1997; *Tartarotti*

20

et al., 2002). Only two occurrences of abyssal peridotites with breakdown plagioclase have been proposed in the literature: Owen Fracture Zone peridotites on the Central Indian Ridge (*Hamlyn and Bonatti*, 1980) and Vema Fracture Zone Peridotites on the MAR (*Cannat and Seyler*, 1995). The Owen Fracture Zone example is based on limited major element data with no trace element data, hence the argument for breakdown is inconclusive. The peridotites from the Vema Fracture Zone are mylonites. If the plagioclase formed by breakdown, this could have been caused by the deformation, as has been observed in an orogenic peridotite (*Newman et al.*, 1999). However, without trace element data for these samples, a melt origin for the plagioclase can not be ruled out in either example.

The characteristics of the plagioclase in the metasomatized peridotites in this study do not exclude a melt origin, though they do require a second, low volume, melt infiltration event after the first event that created the large variations in Cpx trace elements. The fact that the majority of abyssal peridotites do not contain plagioclase leads to the question of why breakdown would occur in any samples. If the trace amounts of plagioclase in the samples in this study formed by spinel breakdown, this reaction was probably triggered by the presence of small amounts of melt. Hence, we conclude that plagioclase in the peridotites either crystallized from a small amount of infiltrating melt or breakdown of spinel was triggered by melt. The occurrence of trace plagioclase in any abyssal peridotite may always be related to very small amounts of melt refertilization. Such a conclusion is in agreement with the Cpx trace element modeling of *Brunelli et al.* (2006), which suggests that all abyssal peridotites have undergone weak refertilization.

Recently, *Borghini et al.* (2009, 2010) have presented an experimentally derived plagioclase barometer, based on anorthite content and temperature:

$$P = 1.05 - 1.71\frac{An}{100} + .000686T \tag{1}$$

where P is pressure in GPa, An is % anorthite, and T is temperature in °C. As the trace element

metasomatism is estimated to have occurred in the temperature range 1000-1200°C, the assumed maximum temperature for plagioclase formation is 1000°C. Average anorthite in 6K-465-2 is 91% and in RC27-9-6-5 is 84% (Table 7). Using a pressure/depth conversion of 1 GPa $\approx$ 30 km, plagioclase is estimated to have a maximum formation depth of 5 km and 9 km, respectively.

Mid-ocean ridge processes

The observation of multiple shallow-level melt impregnation events in four peridotites from the Atlantis II Fracture Zone suggests that melt-rock interaction in the mantle is considerably more important than previously suggested for this area (*Johnson et al.*, 1990; *Johnson and Dick*, 1992; *Coogan et al.*, 2004). However, this observation is in agreement with recent models for oceanic core complex formation (e.g., *Dick et al.*, 2000; *John et al.*, 2004; *Ildefonse et al.*, 2007). Further, the observation of melt impregnation agrees with evidence for the importance of melt-rock interaction in the mantle at other slow and ultra-slow spreading ridges (*Seyler et al.*, 2001, 2004, 2007; *Hellebrand et al.*, 2002; *Brunelli et al.*, 2006). This suggests that the interaction of melts with the mantle through which they migrate is important during the generation of oceanic lithosphere.

Two of the cryptically metasomatized samples (6K-465-2 and RC27-9-6-5) are from the present-day RTI core complex and the other two (6K-458-1 and 6K-458-3) are from the Atlantis Bank fossil core complex, located at 12 Ma along the fracture zone. Oceanic core complexes are uplifted massifs on the seafloor and have been recognized as an important component of the ridge tectonic system (*Cann et al.*, 1997; *Tucholke et al.*, 1998). Spreading at core complexes is accommodated by low angle detachment faulting. Lower crust and upper mantle are uplifted and exposed on one side of the ridge axis, while the hanging wall of the fault transports the basaltic crust in the opposite direction. Models of oceanic core complexes have proposed that they form at slow spreading ridges where magma supply is variable (e.g., *Escartín et al.*, 2003; *Ildefonse et al.*, 2007; *MacLeod et al.*, 2009). In these regions, the oceanic lithosphere consists of gabbro intruded into peridotite,

22

which results in strain localization and detachment faulting.

In Fig. 12, sample averaged Cpx REEs are plotted for dredges and dives from the Atlantis II Fracture Zone RTI and Atlantis Bank. In addition, individual analyses for the cryptically metasomatized peridotites are plotted to demonstrate the large compositional range of these samples. The background light grey field is the range for all other Atlantis II Fracture Zone peridotites along the transform fault (*Johnson and Dick*, 1992), which is much more limited than the range for the two core complexes. Peridotites from the core complexes extend to REE compositions almost as depleted as the most depleted fracture zone samples, but they also extend to an order of magnitude more enriched compositions than other Atlantis II peridotites. This large range in trace element compositions indicates that other processes, such as magmatic intrusion into the mantle, occur at the Atlantis II Fracture Zone, in addition to depletion by fractional melting. This observation is in agreement with the complex magmatic history that is often inferred for these types of massifs (*John et al.*, 2004; *Tucholke et al.*, 2008).

At Atlantis Bank, extensive surveys of the massif have revealed that a large gabbro body makes up the bulk of the core complex (*Dick et al.*, 2000; *John et al.*, 2004). Gabbro represents 52% of recovered dredge and dive material, in addition to a 1.5 km drill core that is entirely gabbroic (*Dick et al.*, 2000). Analyses of the gabbros have demonstrated the occurrence of several magmatic pulses and magmatic differentiation during the >1 My when the core complex was active (*Natland and Dick*, 2002; *John et al.*, 2004; *Baines et al.*, 2009). At least one other study of Atlantis Bank peridotite has found evidence for melt entrapment in the mantle, in the form of a gabbro veined dunite with cross-cutting chromite within a harzburgite (*Morishita et al.*, 2007).

The presence of a large gabbro body at Atlantis Bank provides a general source for the metasomatism of peridotites 6K-458-1 and 6K-458-3. These peridotites were collected approximately 250 m apart on Dive 458, though not in situ (Table 1) and other samples recovered in this dive include oxide gabbros. Hence, 6K-458-1 and 6K-458-3 were probably metasomatized by melt squeezed out of nearby gabbro into the surrounding peridotite. Given that the trace element concentrations

23

of 6K-458-1 and 6K-458-3 form a continuous gradation from depleted to enriched (Fig. 12), the metasomatism of these samples may have been the result of a single event. However, as the metasomatic Cpx do not have significant Zr or Ti depletions compared to residual Cpx, this suggests that the infiltrating melt was not strongly fractionated. Hence, the oxide gabbros from Dive 458 may not be the source of the melt, but instead represent a later episode of melt intrusion. Zircon and apatite dating by *John et al.* (2004) suggest several cycles of melt intrusion in the gabbro at Atlantis Bank. Gabbro crystallization at Atlantis Bank is estimated to have occurred over a temperature range of 700-1000°C, based on Ti-in-zircon thermometry by *Grimes et al.* (2009). This observation is consistent with our estimate for the first episode of peridotite metasomatism occurring in the range 1000-1200°C, if multiple melt intrusion events occurred and the oxide gabbros formed later in the history of this region of Atlantis Bank.

The RTI at Atlantis II Fracture Zone is considerably less studied and less sampled than Atlantis Bank. The two metasomatized peridotites, RC27-9-6-2 and 6K-465-2, were collected at separate locations (Fig. 1) and must have been metasomatized separately. The composition of plagioclase supports this conclusion, as plagioclase in RC27-9-6-5 is estimated to have formed at 9 km depth, based on the *Borghini et al.* (2009) barometer, while plagioclase in 6K-465-2 has a 5 km depth estimate. At both locations, there is direct evidence for melt intrusion into the mantle, in the form of clinopyroxenite- and gabbro-veined peridotites in Dredge RC27-9-6 and olivine gabbros in Dive 465. Hence, similar to Atlantis Bank, the mantle at the present-day RTI has undergone a long history of melt intrusion into the mantle, which has created heterogeneous lithosphere.

Conclusions

Geochemical analyses of abyssal peridotites from the Atlantis II Fracture Zone on the Southwest Indian Ridge reveal the occurrence of cryptic metasomatism in the oceanic lithospheric mantle. Of 14 peridotites analyzed, all appear macroscopically to be residual peridotites, due to the absence

of cross-cutting veins or dunites. In three samples, Cpx grains with typical, depleted trace element concentrations and those with enriched concentrations occur within 1-2 cm of each other. In a fourth sample, Cpx trace element concentrations are uniformly enriched. Compared to the composition of typical residual peridotites, these four samples are enriched in LREE by three orders of magnitude. Co-variation of Ti and Zr in the cryptically metasomatized peridotites indicates that the chemical heterogeneity did not result from various degrees of fractional melting or by direct crystallization from a basaltic melt. Instead, the large variation in trace elements is interpreted to be the result of infiltration by low volume melt fractions.

This study expands the observational length-scale for variations in abyssal peridotite composition down to the single grain ($\sim$1-5 mm) and single rock ($\sim$10-50 cm) scales. In general, Cpx in individual abyssal peridotites are not zoned, either within or among grains. The lack of zonation in the majority of abyssal peridotites suggests that diffusion does not limit the equilibration of Cpx with melt during mantle melting. In the metasomatized peridotites, the small spatial scale of the variations can only be preserved if the metasomatism occurred at shallow depth in the lithospheric mantle. Based on calculations of the timescales for diffusive equilibration, the melt impregnation is estimated to have occurred at depths of 10-20 km and temperatures of 1000-1200°C. Hence, the lithospheric mantle at the ridge axis can be relatively thick at ultra-slow spreading ridges.

In at least two of the metasomatized samples, trace amounts of plagioclase ($<$0.01%) intergrown with spinel, olivine, and pyroxenes are present. Plagioclase may have formed either by crystallizing directly from a low volume infiltrating melt or by breakdown of spinel triggered by the presence of small amounts of melt. In either case, plagioclase formation post-dates the trace element metasomatic event, as both enriched and depleted Cpx have negative Eu anomalies in their rims but not their cores. This observation suggests that melt-rock reaction occurs multiple times and to shallow depths in the mantle.

The Atlantis II Fracture Zone peridotites in this study are located on oceanic core complexes at the present-day RTI and at Atlantis Bank. At both locations, sampling of veined peridotites and

25

gabbros provide evidence for intrusions of melt into the mantle. In particular, studies of Atlantis Bank have found evidence for a prolonged history of magmatic intrusions. Hence, metasomatism of the peridotites in this study probably relates to various shallow-level intrusions of gabbroic melts into the lithospheric mantle during oceanic core complex formation. The lithospheric mantle at ultra-slow spreading ridges can thus be relatively heterogeneous in composition.

Acknowledgements

References

Albee, A. L., and L. Ray (1970), Correction factors for electron probe microanalysis of silicates, oxides, carbonates, phosphates, and sulfates, *Analytical Chemistry*, *42*(12), 1408–1414.

Anders, E., and N. Grevesse (1989), Abundances of the elements: Meteoritic and solar, *Geochimica et Cosmochimica Acta*, *53*, 197–214.

Asimow, P. D., M. M. Hirschmann, M. S. Ghiorso, M. J. O'Hara, and E. M. Stolper (1995), The effect of pressure-induced solid-solid phase transitions on decompression melting of the mantle, *Geochimica et Cosmochimica Acta*, *59*(21), 4489–4506.

Baines, A. G., M. J. Cheadle, H. J. B. Dick, A. Hosford Scheirer, B. E. John, N. J. Kusznir, and T. Matsumoto (2003), Mechanism for generating the anomalous uplift of oceanic core complexes: Atlantis Bank, southwest Indian Ridge, *Geology*, *31*(12), 1105–1108.

Baines, A. G., M. J. Cheadle, H. J. B. Dick, A. Hosford Scheirer, B. E. John, N. J. Kusznir, and T. Matsumoto (2007), Evolution of the Southwest Indian Ridge from 55°45'e to 62°e: Changes in plate-boundary geometry since 26 Ma, *Geochemistry, Geophysics, and Geosystems*, *8*(6), doi:10.1029/2006GC001,559.

Baines, A. G., M. J. Cheadle, B. E. John, and J. J. Schwartz (2008), The rate of oceanic detachment faulting at Atlantis Bank, SW Indian Ridge, *Earth and Planetary Science Letters*, *273*, 105–114.

Baines, A. G., M. J. Cheadle, B. E. John, C. B. Grimes, J. J. Schwartz, and J. L. Wooden (2009), SHRIMP Pb/U zircon ages constrain gabbroic crustal accretion at Atlantis Bank on the ultraslow-spreading Southwest Indian Ridge, *Earth and Planetary Science Letters*, *287*, 540–550.

Batchelor, G. K. (1967), *An Introduction to Fluid Dynamics*, Cambridge University Press.

Bence, A. E., and A. L. Albee (1968), Empirical correction factors for the electron microanalysis of silicates and oxides, *Journal of Geology*, *76*, 382–403.

Bodinier, J.-L., and M. Godard (2003), Orogenic, ophiolitic, and abyssal peridotites, in *Treatise on Geochemistry*, vol. 2, edited by R. W. Carlson, pp. 103–170, Elsevier.

Bodinier, J. L., G. Vasseur, J. Vernieres, C. Dupuy, and J. Fabries (1990), Mechanisms of mantle metasomatism: Geochemical evidence from the Lherz Orogenic Peridotite, *Journal of Petrology*, *31*(3), 597–628.

Borghini, G., E. Rampone, L. Crispini, R. De Ferrari, and M. Godard (2007), Origin and emplacement of ultramafic-mafic intrusions in the Erro-Tobbio mantle peridotite (Ligurian Alps, Italy), *Lithos*, *94*, 210–229.

Borghini, G., P. Fumagalli, and E. Rampone (2009), The composition of plagioclase in mantle peridotites: A geobarometric marker for lithospheric mantle exhumation, in *Alpine Ophiolites and Modern Analogues*.

Borghini, G., P. Fumagalli, and E. Rampone (2010), The stability of plagioclase in the upper mantle: Subsolidus experiments on fertile and depleted lherzolite, *Journal of Petrology*, *This Volume*.

Boudier, F., and A. Nicolas (1995), Nature of the Moho Transition Zone in the Oman Ophiolite, *Journal of Petrology*, *36*(3), 777–796.

Bown, J. W., and R. S. White (1994), Variation with spreading rate of oceanic crustal thickness and geochemistry, *Earth and Planetary Science Letters*, *121*, 435–449.

Brunelli, D., M. Seyler, A. Cipriani, L. Ottolini, and E. Bonatti (2006), Discontinuous melt extraction and weak refertilization of mantle peridotites at the Vema Lithospheric Section (Mid-Atlantic Ridge), *Journal of Petrology*, *47*(4), 745–771.

Cann, J. R., D. K. Blackman, D. K. Smith, E. McAllister, B. Janssen, S. Mello, E. Avgerinos, A. R. Pascoe, and J. Escartin (1997), Corrugated slip surfaces formed at ridge-transform intersections on the Mid-Atlantic Ridge, *Nature*, *385*, 329–332.

Cannat, M., and M. Seyler (1995), Transform tectonics, metamorphic plagioclase and amphibolitization in ultramafic rocks of the Vema transform fault (Atlantic Ocean), *Earth and Planetary Science Letters*, *133*, 283–298.

Cannat, M., D. Bideau, and R. Hébert (1990), Plastic deformation and magmatic impregnation in serpentinized ultramafic rocks from the Garrett transform fault (East Pacific Rise), *Earth and Planetary Science Letters*, *101*(216-232).

Cannat, M., D. Bideau, and H. Bougault (1992), Serpentinized peridotites and gabbros in the Mid-Atlantic Ridge axial valley at 15°37'N and 16°52'N, *Earth and Planetary Science Letters*, *109*, 87–106.

Cherniak, D. J., and Y. Liang (2007), Rare earth element diffusion in natural enstatite, *Geochimica et Cosmochimica Acta*, *71*, 1324–1340.

Constantin, M. (1999), Gabbroic intrusions and magmatic metasomatism in harzburgites from the Garrett transform fault: implications for the nature of the mantle-crust transition at fast-spreading ridges, *Contributions to Mineralogy and Petrology*, *136*, 111–130.

Constantin, M., R. Hékinian, D. Ackermand, and P. Stoffers (1995), Mafic and ultramafic intrusions into upper mantle peridotites from fast spreading centers of the Easter Microplate (South East Pacific), in *Mantle and Lower Crust Exposed in Oceanic Ridges and in Ophiolites*, edited by R. L. M. Vissers and A. Nicolas, pp. 71–120, Kluwer Academic Publishers.

Coogan, L. A., G. M. Thompson, C. J. MacLeod, H. J. B. Dick, S. J. Edwards, A. Hosford Scheirer, and T. L. Barry (2004), A combined basalt and peridotite perspective on 14 million years of melt generation at the Atlantis Bank segment of the Southwest Indian Ridge: evidence for temporal changes in mantle dynamics, *Chemical Geology*, *207*, 13–30.

Dantas, C., G. Ceuleneer, M. Gregoire, M. Python, R. Freydier, J. Warren, and H. J. B. Dick (2007), Pyroxenites from the Southwest Indian Ridge, 9-16°E: Cumulates from incremental melt fractions produced at the top of a cold melting regime, *Journal of Petrology*, *48*(4), 647–660.

Dick, H. J. B. (1989), Abyssal peridotites, very slow spreading ridges and ocean ridge magmatism, in *Magmatism in the Ocean Basins*, edited by A. D. Saunders and M. J. Norry, no. 42 in Special Publication, pp. 71–105, Geological Society of London.

Dick, H. J. B., and T. Bullen (1984), Chromian spinel as a petrogenetic indicator in abyssal and alpine-type peridotites and spatially associated lavas, *Contributions to Mineralogy and Petrology*, *86*, 54–76.

Dick, H. J. B., and J. H. Natland (1996), Late-stage melt evolution and transport in the shallow mantle beneath the East Pacific Rise, in *Proceedings of the Ocean Drilling Program, Scientific Results*, vol. 147, edited by C. Mével, K. M. Gillis, J. F. Allan, and P. S. Meyer, pp. 103–134, College Station, TX.

Dick, H. J. B., R. L. Fisher, and W. B. Bryan (1984), Mineralogic variability of the uppermost mantle along mid-ocean ridges, *Earth and Planetary Science Letters*, *69*, 88–106.

Dick, H. J. B., J. Lin, and H. Schouten (2003), An ultraslow-spreading class of ocean ridge, *Nature*, *426*, 405–412.

Dick, H. J. B., C. J. Lissenberg, and J. M. Warren (2010), Mantle melting, melt transport and delivery beneath a slow-spreading ridge: The paleo-MAR from $23°15'$N to $23°45'$N, *Journal of Petrology*, *this volume*.

Dick, H. J. B., et al. (1991), Tectonic evolution of the Atlantis II Fracture Zone, in *Proceedings of the Ocean Drilling Program, Scientific Results*, vol. 118, edited by R. P. Von Herzen and P. T. Robinson, pp. 359–398, College Station, TX.

Dick, H. J. B., et al. (2000), A long in situ section of the lower ocean crust: results of ODP Leg 176 drilling at the Southwest Indian Ridge, *Earth and Planetary Science Letters*, *179*, 31–51.

Dijkstra, A. H., M. R. Drury, and R. L. M. Vissers (2001), Structural petrology of plagioclase peridotites in the west Othris Mountains (Greece): Melt impregnation in mantle lithosphere, *Journal of Petrology*, *42*, 5–24.

Dijkstra, A. H., M. R. Drury, R. L. M. Vissers, and J. Newman (2002), On the role of melt-rock reaction in mantle shear zone formation in the Othris Peridotite Massif (Geece), *Journal of Structural Geology*, *24*, 1431–1450.

Escartín, J., C. Mével, C. J. MacLeod, and A. M. McCaig (2003), Constraints on deformation conditions and the origin of oceanic detachments: The Mid-Atlantic Ridge core complex at 15°45'N, *Geochemistry, Geophysics, and Geosystems*, *4*(8), doi:10.1029/2002GC000,472.

Fujii, T. (1990), Petrology of peridotites from Hole 670A, Leg 109, in *Proceedings of the Ocean Drilling Program, Scientific Results*, vol. 106/109, edited by R. Detrick, J. Honnorez, W. B. Bryan, T. Juteau, and et al., pp. 19–25, College Station, TX.

Gaetani, G. A., and T. L. Grove (1998), The influence of water on melting of mantle peridotite, *Contributions to Mineralogy and Petrology*, *131*, 323–346.

Ghose, I., M. Cannat, and M. Seyler (1996), Transform fault effect on mantle melting in the MARK area (Mid-Atlantic Ridge south of the Kane transform), *Geology*, *24*(12), 1139–1142.

Godard, M., J.-L. Bodinier, and G. Vasseur (1995), Effects of mineralogical reactions on trace element redistributions in mantle rocks during percolation processes: A chromatographic approach, *Earth and Planetary Science Letters*, *133*, 449–461.

Green, D. H., and W. Hibberson (1970), The instability of plagioclase in peridotite at high pressure, *Lithos*, *3*(3), 209–221.

Grimes, C. B., B. E. John, M. J. Cheadle, F. K. Mazdab, J. L. Wooden, S. Swapp, and J. J. Schwartz (2009), On the occurrence, trace element geochemistry, and crystallization history of zircon from in situ ocean lithosphere, *Contributions to Mineralogy and Petrology*, *158*, 757–783.

Hamlyn, P. R., and E. Bonatti (1980), Petrology of mantle-derived ultramafics from the Owen Fracture Zone, northwest Indian Ocean: Implications for the nature of the oceanic upper mantle, *Earth and Planetary Science Letters*, *48*, 65–79.

Hanghøj, K., P. B. Kelemen, D. Hassler, and M. Godard (2010), Composition and genesis of depleted mantle peridotites from the Wadi Tayin Massif, Oman Ophiolite. major and trace element geochemistry, and Os isotope and PGE systematics, *Journal of Petrology*, *This Volume*.

Hart, S. R., and T. Dunn (1993), Experimental cpx/melt partitioning of 24 trace elements, *Contributions to Mineralogy and Petrology*, *113*, 1–8.

Hellebrand, E., J. E. Snow, H. J. B. Dick, and A. W. Hofmann (2001), Coupled major and trace elements as indicators of the extent of meting in mid-ocean-ridge peridotites, *Nature*, *410*, 677–681.

Hellebrand, E., J. E. Snow, P. Hoppe, and A. W. Hofmann (2002), Garnet-field melting and late-stage refertilization in 'residual' abyssal peridotites from the Central Indian Ridge, *Journal of Petrology*, *43*(12), 2305–2338.

Hofmann, A. W. (1988), Chemical differentiation of the Earth: the relationship between mantle, continental crust, and oceanic crust, *Earth and Planetary Science Letters*, *90*, 297–314.

Hoogerduijn Strating, E. H., E. Rampone, G. B. Piccardo, M. R. Drury, and R. L. M. Vissers (1993), Subsolidus emplacement of mantle peridotites during incipient oceanic rifting and opening of the Mesozoic Tethys (Voltri Massif, NW Italy), *Journal of Petrology*, *34*, 901–927.

Hosford, A., M. Tivey, T. Matsumoto, H. Dick, H. Schouten, and H. Kinoshita (2003), Crustal magnetization and accretion at the Southwest Indian Ridge near the Atlantis II fracture zone, 0-25 Ma, *Journal of Geophysical Research*, *108*(B3), 10.1029/2001JB000,604.

Ildefonse, B., D. K. Blackman, B. E. John, Y. Ohara, D. J. Miller, and C. J. MacLeod (2007), Oceanic core complexes and crustal accretion at slow-spreading ridges, *Geology*, *35*, 623–626.

Irving, A. J., and F. A. Frey (1984), Trace element abundances in megacrysts and their host basalts: Constraints on partition coefficients and megacryst genesis, *Geochimica et Cosmochimica Acta*, *48*, 1201–1221.

Iwamori, H. (1992), Melt-solid flow with diffusion-controlled chemical reaction, *Geophysical Research Letters*, *19*(3), 309–312.

Iwamori, H. (1993), A model for disequilibrium mantle melting incorporating melt transport by porous and channel flows, *Nature*, *366*, 734–737.

Jaroslow, G. E., G. Hirth, and H. J. B. Dick (1996), Abyssal peridotite mylonites: implications for grain-size sensitive flow and strain localization in the oceanic lithosphere, *Tectonophysics*, *256*, 17–37.

Jochum, K. P., D. B. Dingwell, A. Rocholl, B. Stoll, A. W. Hofmann, and et al. (2000), The preparation and preliminary characterisation of eight geological MPI-DING reference glasses for in-situ microanalysis, *Geostandards Newsletter*, *24*(1), 87–133.

John, B. E., D. A. Foster, J. M. Murphy, M. J. Cheadle, A. G. Baines, C. M. Fanning, and P. Copeland (2004), Determining the cooling history of in situ lower oceanic crust − Atlantis Bank, SW Indian Ridge, *Earth and Planetary Science Letters*, *222*, 145–160.

Johnson, K. T. M., and H. J. B. Dick (1992), Open system melting and temporal and spatial variation of peridotite and basalt at the Atlantis II Fracture Zone, *Journal of Geophysical Research*, *97*(B6), 9219–9241.

Johnson, K. T. M., H. J. B. Dick, and N. Shimizu (1990), Melting in the oceanic upper mantle: An ion microprobe study of diopsides in abyssal peridotites, *Journal of Geophysical Research*, *95*, 2661–2678.

Juteau, T., E. Berger, and M. Cannat (1990), Serpentinized, residual mantle peridotites from the M.A.R. median valley, ODP Hole 670A (21°10'N, 45°02'W, Leg 109): Primary mineralogy and geothermometry, in *Proceedings of the Ocean Drilling Program, Scientific Results*, vol. 106/109, edited by R. Detrick, J. Honnorez, W. B. Bryan, T. Juteau, and et al., pp. 27–45, College Station, TX.

Kaczmarek, M.-A., and O. Müntener (2008), Juxtaposition of melt impregnation and high-temperature shear zones in the upper mantle; field and petrological constraints from the Lanzo Peridotite (northern Italy), *Journal of Petrology*, *49*(12), 2187–2220.

Kelemen, P. B., and H. J. B. Dick (1995), Focused melt flow and localized deformation in the upper mantle: Juxtaposition of replacive dunite and ductile shear zones in the Josephine peridotite, SW Oregon, *Journal of Geophysical Research*, *100*(B1), 423–438.

Kelemen, P. B., H. J. B. Dick, and J. E. Quick (1992), Formation of harzburgite by pervasive melt/rock reaction in the upper mantle, *Nature*, *358*, 635–641.

Kelemen, P. B., N. Shimizu, and V. J. M. Salters (1995), Extraction of mid-ocean-ridge basalt from the upwelling mantle by focused flow of melt in dunite channels, *Nature*, *375*, 747–753.

Kinzler, R. J. (1997), Melting of mantle peridotite at pressures approaching the spinel to garnet transition: Application to mid-ocean ridge basalt petrogenesis, *Journal of Geophysical Research*, *102*(B1), 853–874.

Kinzler, R. J., and T. L. Grove (1992), Primary magmas of mid-ocean ridge basalts 2. applications, *Journal of Geophysical Research*, *97*(B5), 6907–6926.

Klein, E. M., and C. H. Langmuir (1987), Global correlations of ocean ridge basalt chemistry with axial depth and crustal thickness, *Journal of Geophysical Research*, *92*(B8), 8089–8115.

Kumagai, H., H. J. B. Dick, and I. Kaneoka (2003), Noble gas signatures of abyssal gabbros and peridotites at an Indian Ocean core complex, *Geochemistry, Geophysics, and Geosystems*, *4*(12), 10.1029/2003GC000,540.

Le Roux, V., J.-L. Bodinier, A. Tommasi, O. Alard, J. M. Dautria, A. Vauchez, and A. J. V. Riches (2007), The Lherz spinel lherzolite: Refertilized rather than pristine mantle, *Earth and Planetary Science Letters*, *259*, 599–612.

Lee, K.-L. (1997), Petrological and geochemical studies of an abyssal peridotite from the Atlantis II Fracture Zone, Master's thesis, MIT/WHOI Joint Program.

Liang, Y. (2003), Kinetics of crystal-melt reaction in partially molten silicates: 1. grain scale processes, *Geochemistry, Geophysics, and Geosystems*, *4*(5), 10.1029/2002GC000,375.

MacLeod, C. J., R. C. Searle, B. J. Murton, J. F. Casey, C. Mallows, S. C. Unsworth, K. L. Achenbach, and M. Harris (2009), Life cycle of oceanic core complexes, *Earth and Planetary Science Letters*, *287*, 333–344.

McKenzie, D. P., and M. J. Bickle (1988), The volume and composition of melt generated by extension of the lithosphere, *Journal of Petrology*, *29*, 625–679.

Menzies, M. A., N. Rogers, A. Tindle, and C. J. Hawkesworth (1987), Metasomatic and enrichment processes in lithospheric peridotites, an effect of asthenosphere-lithosphere interaction, in *Mantle Metasomatism*, edited by M. A. Menzies and C. J. Hawkesworth, pp. 313–361, Academic Press.

Montési, L. G. J., and M. D. Behn (2007), Mantle flow and melting underneath oblique and ultraslow mid-ocean ridges, *Geophysical Research Letters*, *34*, L24,307, doi: 10.1029/2007GL031067.

Morgan, Z., Y. Liang, and P. B. Kelemen (2008), Significance of the concentration gradients associated with dunite bodies in the Josephine and Trinity ophiolites, *Geochemistry, Geophysics, and Geosystems*, *9*(7), doi:10.1029/2008GC001954.

Morishita, T., J. Maeda, S. Miyashita, H. Kumagai, T. Matsumoto, and H. J. B. Dick (2007), Petrology of local concentration of chromian spinel in dunite from the slow-spreading Southwest Indian Ridge, *European Journal of Mineralogy*, *19*, 871–882.

Müntener, O., and G. B. Piccardo (2003), Melt migration in ophiolitic peridotites: the message from Alpine-Apennine peridotites and implications for embryonic ocean basins, in *Ophiolites in Earth History*, *Special Publication*, vol. 218, edited by Y. Dilek and P. T. Robinson, pp. 69–89, Geological Society of London.

Natland, J. H., and H. J. B. Dick (2002), Stratigraphy and composition of gabbros drilled in Ocean Drilling Program Hole 735B, Southwest Indian Ridge: a synthesis of geochemical data, in *Proceedings of the Ocean Drilling Program, Scientific Results*, vol. 176, edited by J. H. Natland, H. J. B. Dick, D. J. Miller, and R. P. Von Herzen, pp. 1–69, doi: 10.2973/odp.proc.sr.176.002.2002.

Navon, O., and E. Stolper (1987), Geochemical consequences of melt percolation: the upper mantle as a chromatographic column, *Journal of Geology*, *95*, 285–307.

Newman, J., W. M. Lamb, M. R. Drury, and R. L. M. Vissers (1999), Deformation processes in a peridotite shear zone: reaction-softening by an H_2O-deficient, continuous net transfer reaction, *Tectonophysics*, *303*, 193–222.

Python, M., and G. Ceuleneer (2003), Nature and distribution of dykes and related melt migration structures in the mantle section of the Oman ophiolite, *Geochemistry, Geophysics, and Geosystems*, *4*(7), 10.1029/2002GC000,354.

Qin, Z. (1992), Disequilibrium partial melting model and its implications for trace element fractionations during mantle melting, *Earth and Planetary Science Letters*, *112*, 75–90.

Sen, G., F. A. Frey, N. Shimizu, and W. P. Leeman (1993), Evolution of the lithosphere beneath Oahu, Hawaii: rare earth element abundances in mantle xenoliths, *Earth and Planetary Science Letters*, *119*, 53–69.

33

Sen, G., H.-J. Yang, and M. Ducea (2003), Anomalous isotopes and trace element zoning in pla-gioclase peridotite xenoliths of Oahu (Hawaii): implications for the Hawaiian plume, *Earth and Planetary Science Letters*, *207*, 23–38.

Seyler, M., and E. Bonatti (1997), Regional-scale melt-rock interaction in lherzolitic mantle in the Romanche Fracture Zone (Atlantic Ocean), *Earth and Planetary Science Letters*, *146*, 273–287.

Seyler, M., M. J. Toplis, J.-P. Lorand, A. Luguet, and M. Cannat (2001), Clinopyroxene microtex-tures reveal incompletely extracted melts in abyssal peridotites, *Geology*, *29*(2), 155–158.

Seyler, M., J.-P. Lorand, M. J. Toplis, and G. Godard (2004), Asthenospheric metasomatism be-neath the mid-ocean ridge: Evidence from depleted abyssal peridotites, *Geology*, *32*(4), 301–304.

Seyler, M., J.-P. Lorand, H. J. B. Dick, and M. Drouin (2007), Pervasive melt percolation reactions in ultra-depleted refractory harzburgites at the Mid-Atlantic Ridge, 15°20'N: ODP Hole 1274A, *Contributions to Mineralogy and Petrology*, *153*, 303–319.

Shimizu, N., M. P. Semet, and C. J. Allègre (1978), Geochemical applications of quantitative ion-microprobe analysis, *Geochimica et Cosmochimica Acta*, *42*, 1321–1334.

Sneeringer, M., S. R. Hart, and N. Shimizu (1984), Strontium and samarium diffusion in diopside, *Geochimica et Cosmochimica Acta*, *48*, 1589–1608.

Suhr, G., E. Hellebrand, J. E. Snow, and H. A. Seck (2003), Significance of large, refractory dunite bodies in the upper mantle of the Bay of Islands Ophiolite, *Geochemistry, Geophysics, and Geosystems*, *4*(3), doi:10.1029/2001GC000277.

Takahashi, E. (1986), Melting of a dry peridotite KLB-1 up to 14 GPa: Implications on the origin of peridotitic upper mantle, *Journal of Geophysical Research*, *91*(B9), 9367–9382.

Takazawa, E., F. A. Frey, N. Shimizu, M. Obata, and J. L. Bodinier (1992), Geochemical evidence for melt migration and reaction in the upper mantle, *Nature*, *359*, 55–58.

Tartarotti, P., S. Susini, P. Nimis, and L. Ottolini (2002), Melt migration in the upper mantle along the Romanche Fracture Zone (Equatorial Atlantic), *Lithos*, *63*, 125–149.

Tucholke, B. E., J. Lin, and M. C. Kleinrock (1998), Megamullions and mullion structure defin-ing oceanic metamorphic core complexes on the Mid-Atlantic Ridge, *Journal of Geophysical Research*, *103*(B5), 9857–9866.

Tucholke, B. E., M. D. Behn, W. R. Buck, and J. Lin (2008), Role of melt supply in oceanic detachment faulting and formation of megamullions, *Geology*, *36*(6), 455–458.

Van der Wal, D., and J.-L. Bodinier (1996), Origin of the recrystallisation front in the Ronda peridotite by km-scale pervasive porous melt flow, *Contributions to Mineralogy and Petrology*, *122*, 387–405.

34

Van Orman, J. A., T. L. Grove, and N. Shimizu (2001), Rare earth element diffusion in diopside: influence of temperature, pressure, ionic radius, and an elastic model for diffusion in silicates, *Contributions to Mineralogy and Petrology*, *141*, 687–703.

Van Orman, J. A., T. L. Grove, and N. Shimizu (2002), Diffusive fractionation of trace elements during production and transport of melt in earth's upper mantle, *Earth and Planetary Science Letters*, *198*, 93–112.

Vernières, J., M. Godard, and J.-L. Bodinier (1997), A plate model for the simulation of trace element fractionation during partial melting and magma transport in the Earth's upper mantle, *Journal of Geophysical Research*, *102*(B11), 2471–24,784.

Warren, J. M., N. Shimizu, C. Sakaguchi, H. J. B. Dick, and E. Nakamura (2009), An assessment of upper mantle heterogeneity based on abyssal peridotite isotopic compositions, *Journal of Geophysical Research*, *in press*.

Wood, B. J., and J. D. Blundy (2003), Trace element partitioning under crustal and uppermost mantle conditions: The influences of ionic radius, cation charge, pressure, and temperature, in *Treatise on Geochemistry*, vol. 2, edited by R. W. Carlson, pp. 395–424, Elsevier.

Workman, R. K., and S. R. Hart (2005), Major and trace element composition of the depleted MORB mantle (DMM), *Earth and Planetary Science Letters*, *231*, 53–72.
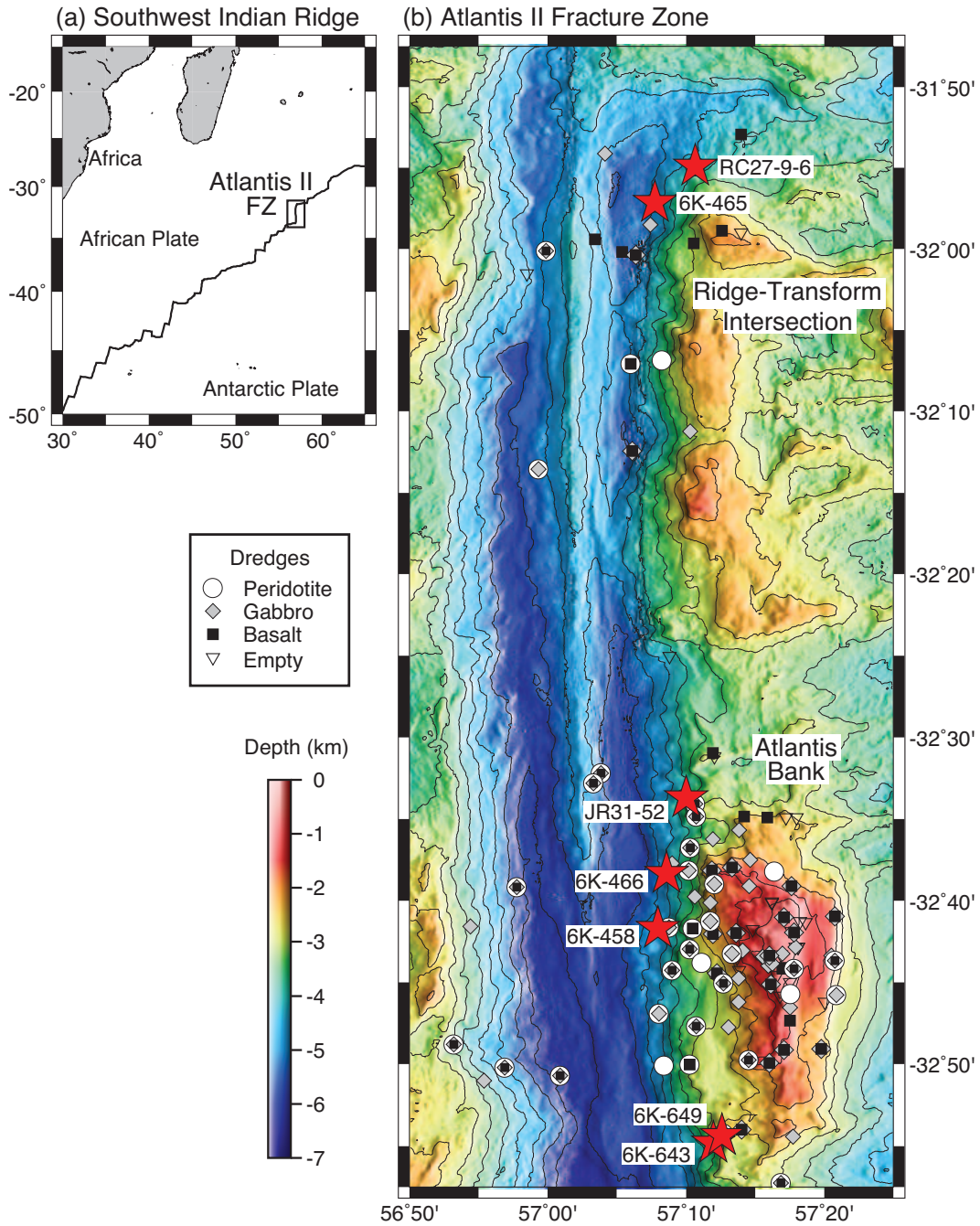
Figure 1: Map of the Atlantis II Fracture Zone with locations of samples (red stars) used in this study. Samples are from the active ridge-transform intersection and from Atlantis Bank, located at 12 Ma along the fracture zone. Spreading is asymmetrical, with a half spreading rate to the south of 8.7 mm/yr and a full spreading rate of 14.1 mm/yr (*Hosford et al.*, 2003; *Baines et al.*, 2007). *Baines et al.* (2008) estimate that from 10.3-12.7 Ma, during the formation of Atlantis Bank, the full spreading rate was higher (15.7 mm/yr) and more asymmetrical, with a half spreading rate to the south of 14.1 mm/yr.
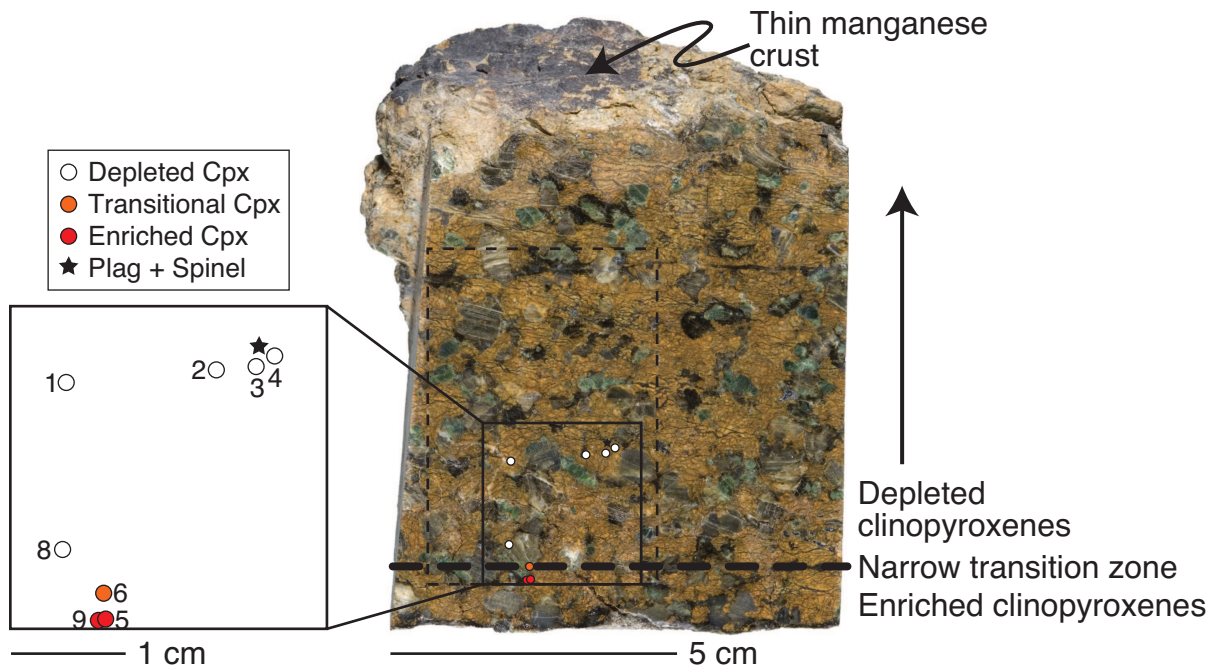
Figure 2: Photograph of cryptically metasomatized peridotite 6K-465-2 from the ridge-transform intersection of the Atlantis II Fracture Zone. The hand specimen looks like a typical residual abyssal peridotite and has no unusual characteristics such as melt veins. However, Cpx LREE concentrations vary across the sample by 2-3 orders of magnitude. The dashed box indicates the area of the rock studied by thin section, with circles to indicate the location of Cpx analyses. As the thin section was cut 2 cm higher than the surface of the slab shown here, Cpx analytical locations do not necessarily correspond to Cpx in the photograph. The solid box is enlarged to show the location of Cpx grains analyzed for trace elements by ion microprobe. Numbers correspond to Cpx grain numbers in Tables 3 and 8. The star indicates the location of the spinel and plagioclase cluster shown in Fig. 3d. The transition from depleted Cpx (low LREE concentrations) to enriched Cpx (high LREE concentrations) occurs over a distance of <1 cm. Photo courtesy of Tom Kleindinst.
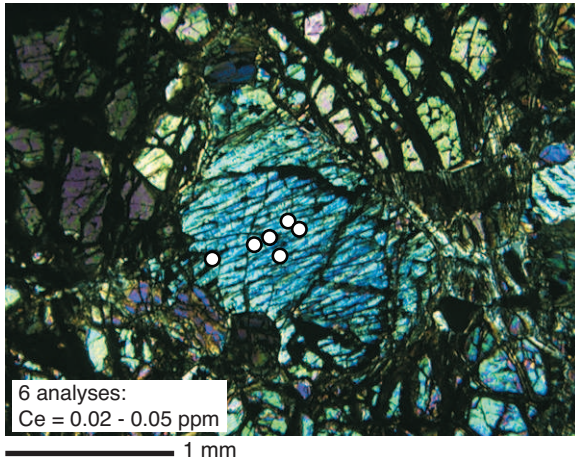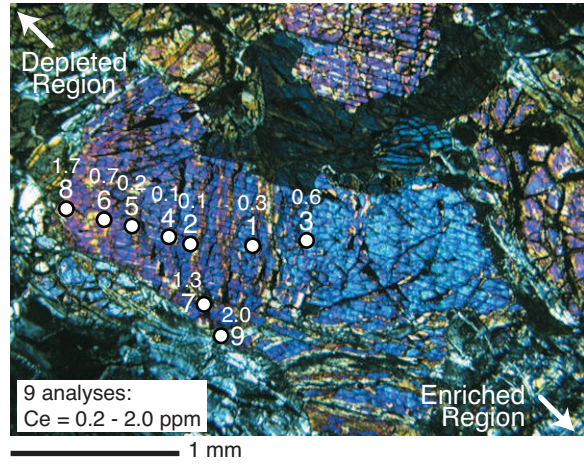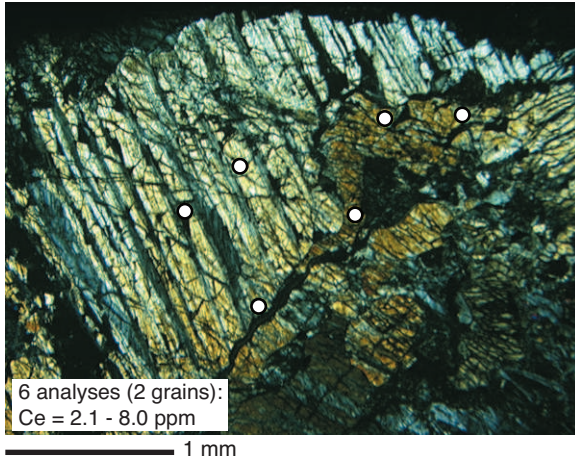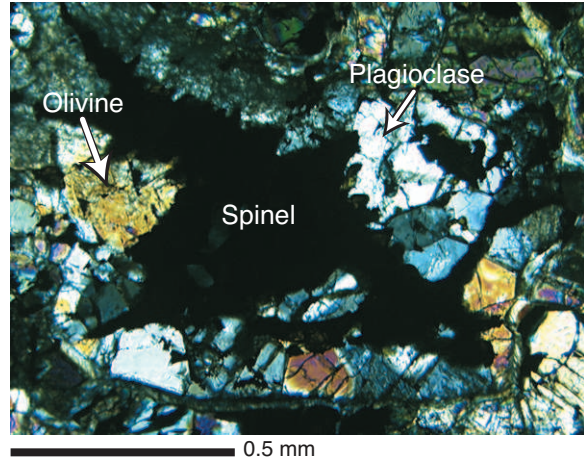
Figure 3: Photomicrographs from cryptically metasomatized peridotite 6K-465-2; white dots indicate trace element analysis locations. **(a)** Photomicrograph of Cpx 2, a porphyroclast from the depleted portion of the peridotite, surrounded by olivine and serpentine. **(a)** Photomicrograph of compositionally zoned Cpx 6, located in the transition zone between the depleted and enriched regions of the peridotite. The grain is surrounded by olivine, Cpx and serpentine. Numbering of analytical points corresponds to the numbering in Tables 3 and 8. Smaller numbers are Ce concentrations in ppm. The lowest trace element concentrations are centered around Point 4. Point 3, while appearing to be near the gain center, has higher concentrations, suggesting that in the third dimension it is closer to the grain rim. **(c)** Photomicrograph of Cpx 5 (large porphyroclast) and Cpx 9 (smaller, darker grain), from the enriched portion of the peridotite. Grains are adjacent to olivine, Cpx and serpentine. **(d)** Photomicrograph of a spinel, plagioclase and olivine cluster, located in the depleted portion of the peridotite, as shown in Fig. 2.
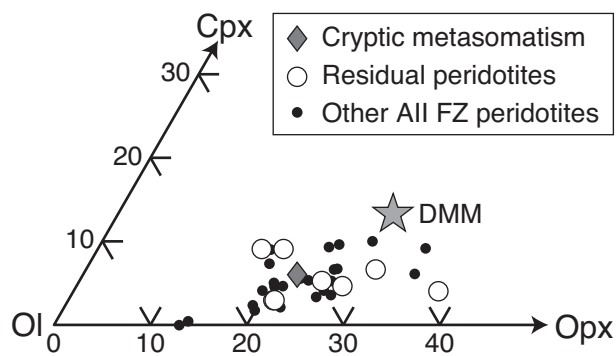
Figure 4: Modal composition of abyssal peridotites in this study compared to other Atlantis II Fracture Zone peridotites. Data for other peridotites are from *Johnson and Dick* (1992), *Kumagai et al.* (2003) and *Morishita et al.* (2007). The modal composition of DMM is from *Workman and Hart* (2005). The cryptically metasomatized peridotite has a modal composition similar to other Atlantis II peridotites.
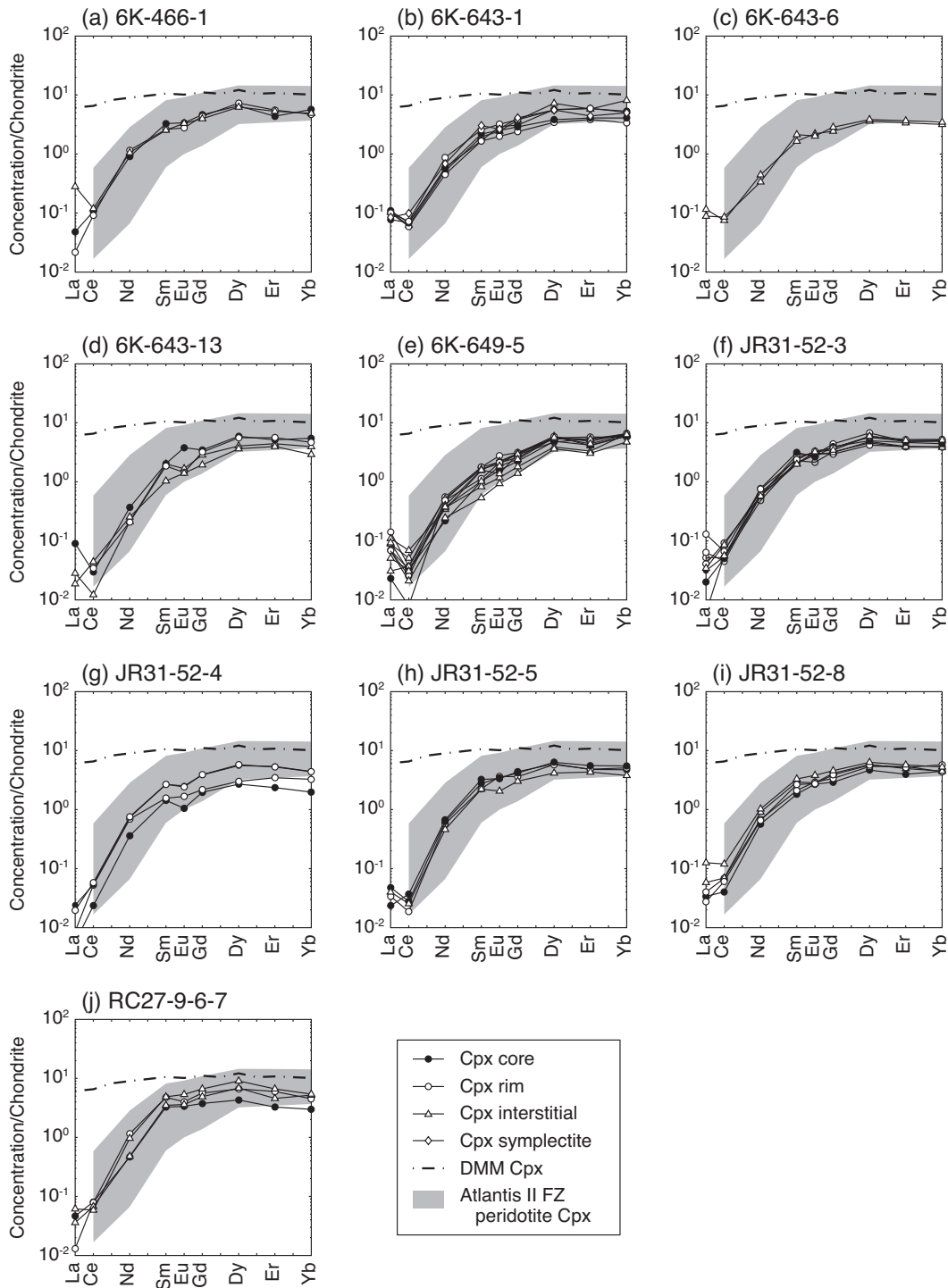
Figure 5: Variation of REEs in Cpx from the residual abyssal peridotites in this study. Data are normalized to chondrite (*Anders and Grevesse*, 1989); the composition of Cpx in DMM is from *Workman and Hart* (2005); the background dataset is Atlantis II Fracture Zone peridotite Cpx from *Johnson and Dick* (1992).
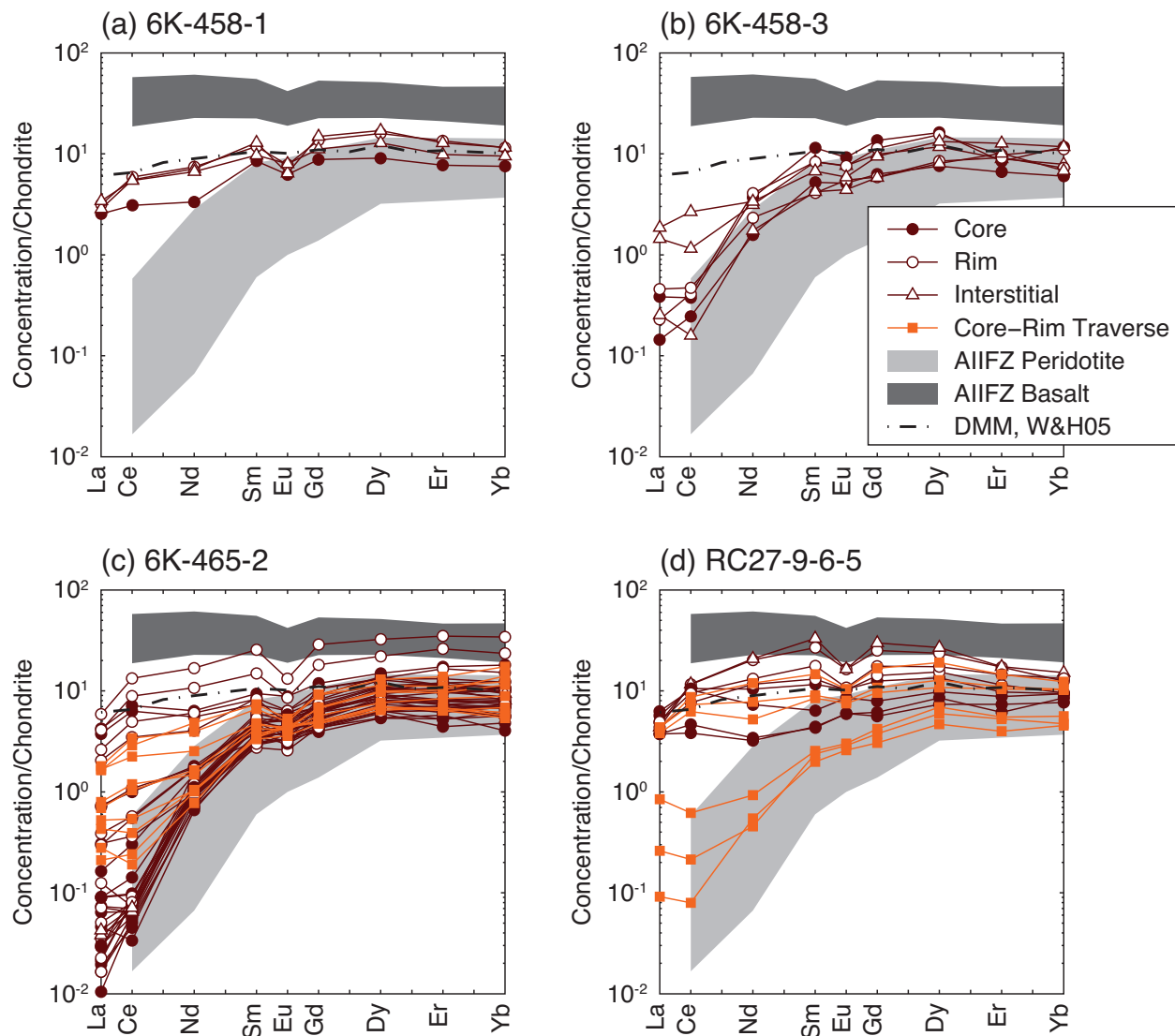
Figure 6: Variation of REEs in Cpx from the cryptically metasomatized peridotites. Core to rim traverses of a single Cpx grain in 6K-465-2 and in RC27-9-6-5 are shown in orange. In both grains, the most depleted analyses are in the core and concentrations increase towards the rim. In 6K-465-2, this Cpx is spatially located between depleted and enriched Cpx grains. Analysis locations for this grain are shown in Figure 3c. Data are normalized to chondrite using *Anders and Grevesse* (1989) and the background fields are the Atlantis II Fracture Zone peridotite and basalt datasets from *Johnson and Dick* (1992).
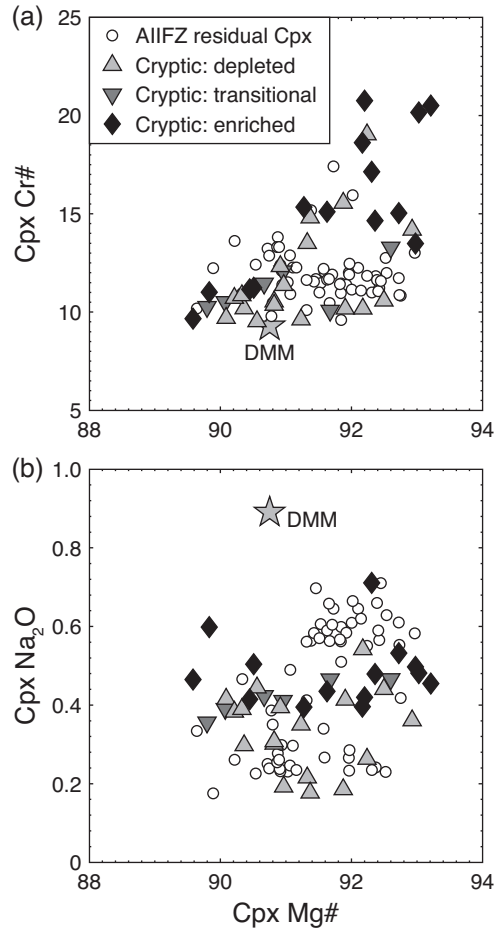
Figure 7: Variation of Mg# with Cr# and Na₂O in Cpx, for residual and cryptically metasomatized peridotites from the Atlantis II Fracture Zone. Additional data from *Johnson et al.* (1990), *Johnson and Dick* (1992), *Coogan et al.* (2004) and *Morishita et al.* (2007); the composition of DMM Cpx is from *Workman and Hart* (2005).
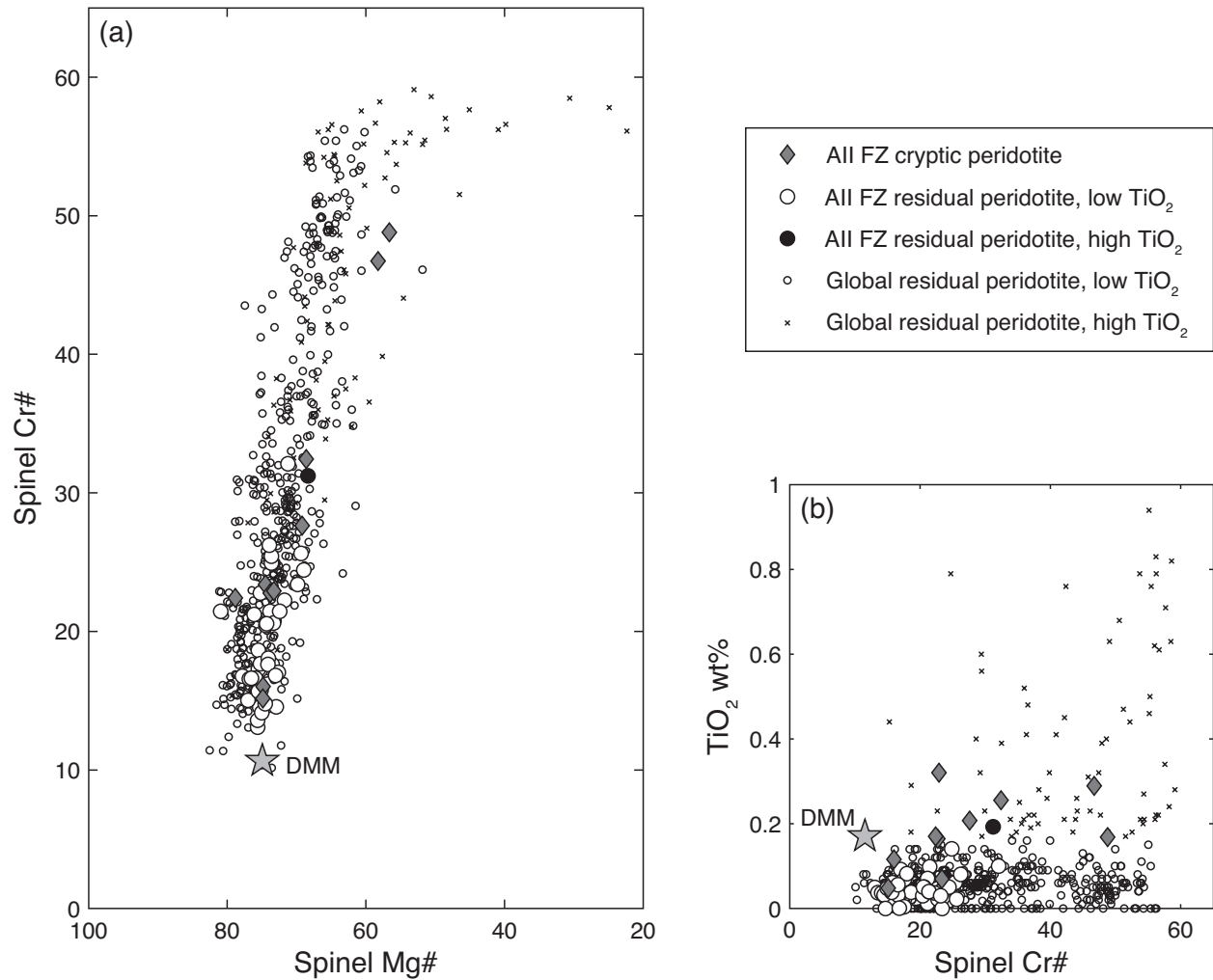
Figure 8: Variations in spinel Cr#, Mg# and TiO_2 in peridotites from the Atlantis II Fracture Zone compared to the global abyssal peridotite dataset. The cryptically metasomatized peridotites have large variations in spinel Cr#, Mg# and TiO_2 (Table 6). Additional Atlantis II Fracture Zone data are from *Johnson et al.* (1990), *Johnson and Dick* (1992), *Jaroslow et al.* (1996), *Coogan et al.* (2004) and *Morishita et al.* (2007); the composition of DMM spinel is from *Workman and Hart* (2005); the global dataset is from a literature compilation.
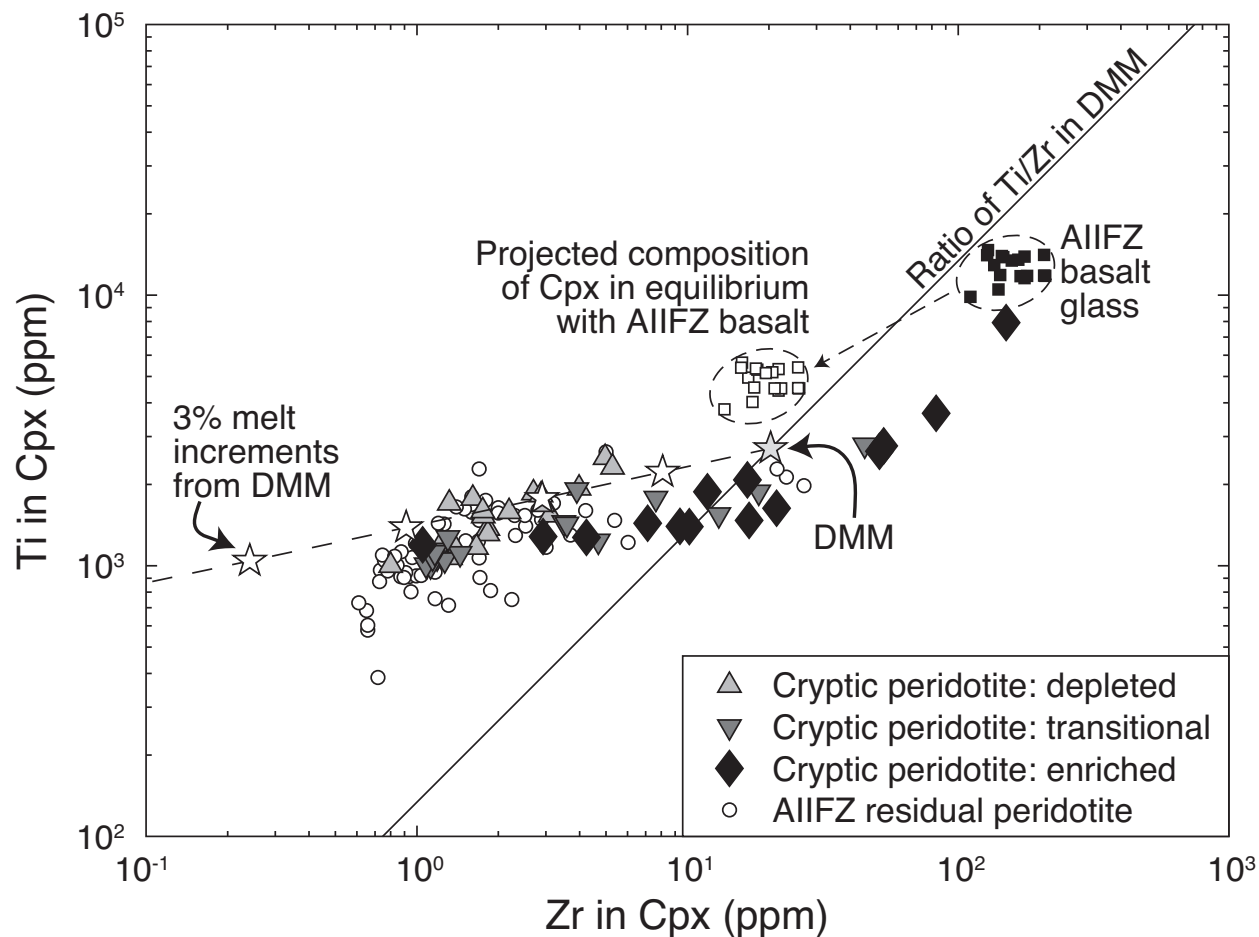
Figure 9: Co-variation of Ti and Zr in peridotite Cpx and basalt glass from the Atlantis II Fracture Zone. Basalt data from *Coogan et al.* (2004); additional Cpx data from *Johnson et al.* (1990) and *Johnson and Dick* (1992). The melting trend, labeled for 3% fractional melting increments, was calculated using melt modes from *Kinzler* (1997), partition coefficients from *Hart and Dunn* (1993) and the composition of Cpx in DMM from *Workman and Hart* (2005). The solid line indicates the variation of Ti with Zr at a constant DMM Ti:Zr ratio. Cryptically metasomatized Cpx do not lie on the melting trend and are also not in equilibrium with basalts from the fracture zone.
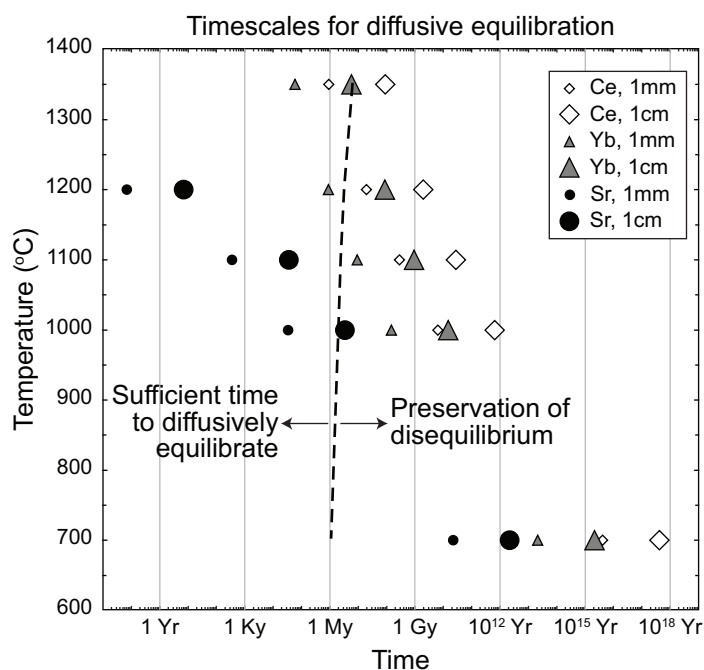
Figure 10: Time-scales for diffusive equilibration of Ce, Yb, and Sr in Cpx as a function of temperature. This calculation is for Cpx with 1 mm radius (smaller symbols) and 1 cm radius (larger symbols), which is equivalent to the minimum and maximum length-scales over which disequilibrium is observed in the metasomatized peridotites. The calculations are based on experimental diffusion datasets from *Van Orman et al.* (2001) for Ce and Yb, and from *Sneeringer et al.* (1984) for Sr. The pressure for the calculations was determined based on the temperature, half spreading rate, and scaling relations from *Montési and Behn* (2007) for the thermal structure of an ultra-slow ridge. The dashed line represents the upwelling time to reach the seafloor starting at a given temperature/depth, calculated from the *Montési and Behn* (2007) scaling relations and the solution for corner flow beneath a ridge axis (*Batchelor*, 1967).
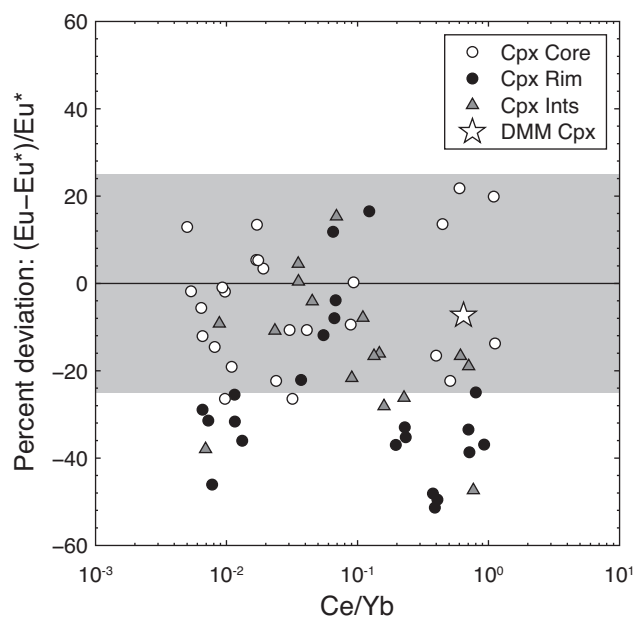
Figure 11: Eu anomalies in Cpx from the three cryptically metasomatized peridotites. Ints refers to interstitial Cpx, whereas Core and Rim refer to Cpx porphyroclasts. Eu* is the predicted Eu concentration based on Sm and Dy concentrations in a Cpx grain. The solid line indicates the absence of an anomaly and the grey shaded box is $\pm$ 25% error, within which Eu anomalies are not significant. The ratio Ce/Yb provides a measure of the relative depletion or enrichment of Cpx. Rims of Cpx from both depleted and enriched regions of the peridotite have significant negative anomalies (i.e., >-25% deviation), whereas cores and interstitial grains typically have no Eu anomaly.
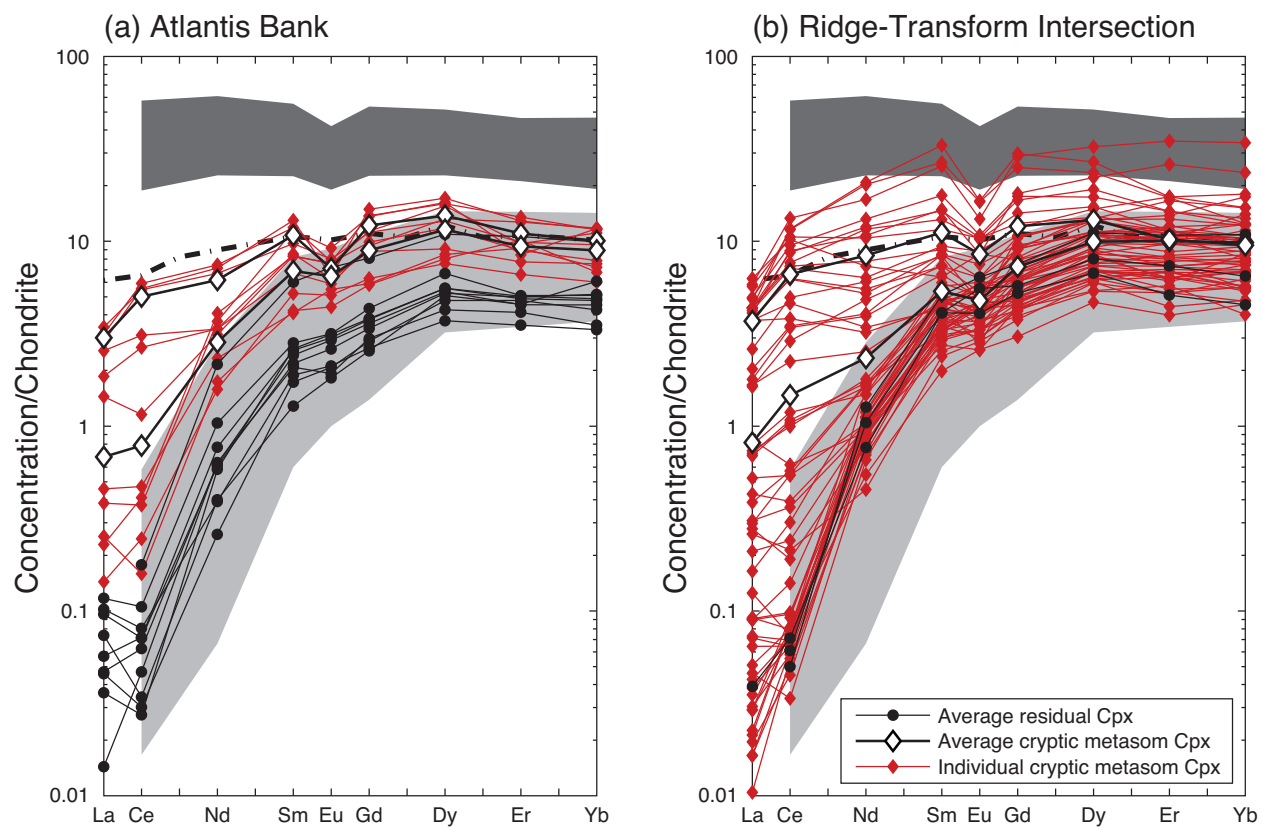
Figure 12: Atlantis II Fracture Zone REE variations at (a) Atlantis Bank and (b) the ridge-transform intersection. Residual peridotites are shown as sample averages. Both average and individual analyses are shown for the cryptically metasomatized peridotites. The averages in (a) are for 6K-458-1 and 6K-458-3 and in (b) are for 6K-465-2 and RC27-9-6-5. Data are chondrite normalized (*Anders and Grevesse*, 1989) and background fields are the Atlantis II Fracture Zone datasets for peridotites (light grey) and basalts (dark grey) from *Johnson and Dick* (1992).

Table 1: Atlantis II Fracture Zone Sample Locations

Dredge/Dive	Outcrop Type	Wt kg	Lat °S	Long °E	Depth (m)	FSR[a] (mm/yr)	Locality
R/V Conrad, 1986							
RC27-9-6	Dredge	37	-31.92	57.18	3930	14	AIIFZ RTI[b]
R.R.S. James Clark Ross, 1998							
JR31-52	Dredge	125	-32.56	57.17	3200	14	Atlantis Bank
R/V Yokosuka, Shinkai 6500 submersible, 1998							
6K-458-1	Float in sediment	3	-32.69	57.13	4867	14	Atlantis Bank
6K-458-3	On outcrop	8	-32.69	57.13	4609	14	Atlantis Bank
6K-465-2	Float in sediment	10	-31.95	57.13	4988	14	AIIFZ RTI
6K-466-1	Float in sediment	3	-32.64	57.14	4714	14	Atlantis Bank
R/V Yokosuka, Shinkai 6500 submersible, 2001							
6K-643-1	From outcrop	9	-32.91	57.20	3396	14	Atlantis Bank
6K-643-6	On outcrop	2	-32.91	57.21	2974	14	Atlantis Bank
6K-643-13	Talus	13	-32.91	57.21	2712	14	Atlantis Bank
6K-649-5	From outcrop	3	-32.91	57.21	2564	14	Atlantis Bank

[a] Full spreading rate: due to asymmetrical spreading, the half spreading rate to the south is 14.1 mm/yr (*Baines et al.*, 2008).

[b] Ridge-transform intersection.

Table 2: Sample descriptions and modal analyses

Sample	Loc.[a]	Description	Oliv	Opx	Cpx	Spin	Plag	Total	Points[b]
RC27-9-6-5[c]	RTI	Lherz, cryptic metasomatism							
RC27-9-6-7	RTI	Lherzolite							
JR31-52-3	AB	Harzburgite	57.6	37.5	3.9	1.0	0.00	100.0	2056
JR31-52-4	AB	Lherzolite							
JR31-52-5	AB	Harzburgite	66.8	27.3	4.5	1.4	0.00	100.0	2258
JR31-52-8	AB	Lherzolite	62.8	29.9	6.5	0.8	0.00	100.0	1975
6K-458-1	AB	Perid, cryptic metasomatism							
6K-458-3	AB	Perid, cryptic metasomatism							
6K-465-2[c]	RTI	Lherz, cryptic metasomatism	71.0	22.0	5.9	1.1	0.01	100.0	1926
6K-466-1	AB	Harzburgite	74.8	21.2	3.0	1.1	0.00	100.0	1489
6K-643-1[d]	AB	Lherzolite	74	17	9	0.5		100.5	
6K-643-6[d]	AB	Harzburgite	75	21	3	0.5		99.5	
6K-643-13	AB	Lherzolite	68.7	24.9	5.1	0.7	0.00	99.4	1566
6K-649-5[d]	AB	Lherzolite	71	19	9	0.5		99.5	

[a] Location is either the ridge-transform intersection (RTI) or Atlantis Bank (AB).

[b] Points counted on 51 by 75 mm thin sections using a 1 mm grid.

[c] Contains trace amounts of plagioclase ($\leq$0.01%).

[d] Modal analysis from *Morishita et al.* (2007).

Table 3: Major element compositions of Cpx, in wt%.

Analysis	Grn[a]	Pts	SiO$_2$	±	TiO$_2$	±	Al$_2$O$_3$	±	Cr$_2$O$_3$	±	FeO	±	MnO	±	MgO	±	CaO	±	Na$_2$O	±	Total	Notes[b]
6K-458-1	1C	9	51.38	0.76	0.23	0.02	5.69	1.19	1.50	0.13	2.20	0.11	0.10	0.02	15.70	0.38	23.12	0.29	0.53	0.04	100.44	Enr
6K-458-1	1R	8	52.36	1.81	0.26	0.08	5.28	1.34	1.35	0.26	2.77	1.42	0.10	0.03	18.77	6.48	19.69	8.07	0.48	0.20	101.05	Enr
6K-458-1	2I	9	51.92	0.59	0.33	0.03	5.37	0.72	1.25	0.05	2.22	0.13	0.10	0.03	16.47	0.30	22.77	0.88	0.50	0.07	100.93	Enr
6K-458-1	3I	9	52.43	0.48	0.31	0.05	4.14	0.60	1.56	0.13	2.21	0.13	0.10	0.03	16.51	0.26	23.24	0.19	0.48	0.03	100.98	Enr
6K-458-3	1I	10	52.09	0.34	0.32	0.02	4.71	0.22	0.80	0.02	2.51	0.15	0.09	0.01	15.97	0.15	22.54	0.55	0.41	0.04	99.43	
6K-458-3	2I	12	52.21	0.28	0.27	0.01	5.66	0.09	0.95	0.05	2.53	0.18	0.09	0.02	15.66	0.39	22.73	0.69	0.47	0.05	100.57	Trans
6K-458-3	3C	13	51.43	1.36	0.24	0.08	7.09	1.05	1.11	0.21	3.21	1.54	0.10	0.03	17.30	5.37	19.68	7.70	0.44	0.16	100.60	Dep
6K-458-3	3R	8	52.78	0.38	0.45	0.05	3.77	0.42	0.93	0.08	2.22	0.07	0.07	0.01	16.34	0.42	23.76	0.38	0.36	0.03	100.67	Dep
6K-458-3	4C	9	51.41	0.68	0.20	0.05	6.48	0.17	1.04	0.06	3.57	0.87	0.11	0.02	18.22	3.15	18.06	4.09	0.42	0.14	99.50	Dep
6K-458-3	4R	8	50.96	0.62	0.27	0.04	6.20	0.55	1.05	0.03	2.36	0.18	0.07	0.01	15.58	0.86	22.51	0.93	0.54	0.18	99.55	Dep
6K-458-3	5I	11	51.69	0.43	0.32	0.04	5.22	0.42	0.92	0.06	2.24	0.12	0.06	0.02	15.47	0.42	23.07	0.31	0.44	0.05	99.42	Dep
6K-458-3	6I	10	51.96	0.31	0.43	0.02	4.50	0.66	1.03	0.03	2.21	0.09	0.10	0.01	15.49	0.42	23.29	0.26	0.47	0.06	99.46	Trans
6K-465-2	1C	8	50.64	0.59	0.23	0.04	6.24	0.06	1.10	0.05	3.13	0.68	0.11	0.02	17.38	2.89	20.57	3.81	0.30	0.09	99.69	Dep
6K-465-2	1R	13	51.99	0.56	0.30	0.02	3.66	0.38	1.28	0.05	2.49	0.17	0.05	0.02	16.64	0.51	23.02	0.81	0.26	0.05	99.71	Dep
6K-465-2	2C	10	51.18	0.39	0.21	0.03	6.45	0.06	1.09	0.04	3.25	0.55	0.03	0.03	17.10	2.25	20.63	3.06	0.30	0.06	100.23	Dep
6K-465-2	2R	10	51.72	0.52	0.24	0.03	5.57	0.42	0.96	0.06	3.07	0.47	0.04	0.02	17.05	1.83	21.50	2.58	0.31	0.06	100.46	Dep
6K-465-2	3C	8	51.25	0.15	0.25	0.04	5.38	0.52	1.03	0.02	2.90	0.13	0.06	0.02	16.40	0.23	22.98	0.63	0.19	0.06	100.45	Dep
6K-465-2	3R	8	51.33	0.48	0.33	0.02	4.75	0.21	1.11	0.03	2.81	0.18	0.07	0.02	16.59	0.63	22.95	0.89	0.22	0.05	100.16	Dep
6K-465-2	4C	10	51.91	0.34	0.26	0.04	4.15	0.40	1.14	0.04	2.67	0.16	0.07	0.01	16.92	0.27	23.01	0.47	0.19	0.04	100.30	Dep
6K-465-2	4R	10	51.60	0.65	0.30	0.03	4.40	0.51	1.14	0.03	2.80	0.12	0.06	0.02	16.62	0.54	22.90	0.70	0.18	0.05	99.99	Dep
6K-465-2	5C	10	50.45	0.43	0.24	0.03	6.41	0.56	1.20	0.03	3.01	0.09	0.10	0.02	15.98	0.30	22.37	0.33	0.41	0.06	100.17	Enr
6K-465-2	6C	9	51.38	0.54	0.18	0.04	6.04	0.34	1.06	0.04	3.78	0.45	0.11	0.01	19.24	2.14	18.03	2.79	0.39	0.05	100.20	Trans
6K-465-2	6R	9	51.15	1.11	0.26	0.06	5.35	0.26	1.10	0.13	2.98	1.18	0.10	0.03	16.84	4.98	21.66	6.63	0.41	0.15	99.85	Trans
6K-465-2	8C	15	51.34	0.49	0.20	0.02	6.46	0.16	1.15	0.03	3.51	0.15	0.10	0.01	18.15	0.43	19.43	0.45	0.38	0.05	100.72	Dep
6K-465-2	8R	18	51.08	1.23	0.26	0.08	5.55	0.31	1.16	0.13	2.84	1.37	0.10	0.02	15.97	5.63	22.89	7.71	0.39	0.20	100.25	Dep
6K-465-2	9C	8	52.59	0.57	0.25	0.03	3.23	0.52	1.26	0.03	2.56	0.08	0.10	0.02	17.01	0.49	23.08	0.24	0.42	0.05	100.51	Enr
6K-465-2	9R	10	52.37	0.75	0.31	0.05	3.52	0.85	1.20	0.11	2.55	0.07	0.11	0.02	16.82	0.39	23.04	0.43	0.40	0.05	100.29	Enr
6K-466-1	1C	10	51.97	0.29	0.26	0.02	5.55	0.10	1.16	0.03	2.51	0.34	0.04	0.02	16.42	1.16	21.88	1.49	0.64	0.05	100.44	
6K-466-1	1R	10	51.94	0.29	0.29	0.02	5.34	0.33	1.19	0.06	2.14	0.06	0.04	0.02	15.89	0.22	23.21	0.22	0.58	0.05	100.64	
6K-466-1	3I	13	52.16	0.93	0.25	0.06	5.18	0.36	1.02	0.18	2.98	1.05	0.13	0.03	17.90	4.56	19.72	5.84	0.70	0.14	100.05	
6K-643-13	1I	8	51.78	0.30	0.15	0.02	5.14	0.15	1.05	0.04	2.79	0.20	0.10	0.02	17.03	0.47	21.90	0.63	0.27	0.04	100.20	
6K-643-13	2C	10	51.39	0.94	0.13	0.04	6.15	0.22	1.28	0.12	4.03	1.12	0.12	0.02	20.10	4.98	16.47	6.97	0.18	0.09	99.84	
6K-643-13	2R	10	51.43	0.43	0.14	0.02	5.76	0.07	1.21	0.03	3.11	0.35	0.11	0.02	17.47	1.62	20.44	2.17	0.23	0.04	99.90	
JR31-52-3	4C	12	51.13	0.31	0.18	0.02	6.46	0.10	1.25	0.04	2.66	0.22	0.08	0.01	16.12	0.80	21.46	0.88	0.61	0.05	99.95	
JR31-52-3	4R	10	51.25	0.32	0.18	0.01	6.25	0.08	1.20	0.05	2.60	0.13	0.08	0.02	16.40	0.63	21.27	0.74	0.60	0.03	99.82	
JR31-52-3	5C	12	51.73	0.59	0.15	0.04	6.53	0.16	1.20	0.11	3.69	1.06	0.09	0.02	19.35	3.94	16.93	5.34	0.47	0.18	100.12	
JR31-52-3	5R	12	50.81	0.39	0.19	0.02	6.65	0.10	1.30	0.04	2.60	0.20	0.07	0.03	15.97	0.77	21.54	1.02	0.59	0.05	99.72	
JR31-52-3	6I	12	51.21	0.21	0.20	0.02	6.54	0.06	1.27	0.04	2.63	0.13	0.08	0.03	15.75	0.39	21.66	0.51	0.58	0.05	99.93	
JR31-52-3	7C	11	51.30	0.49	0.18	0.01	6.06	0.08	1.22	0.02	2.62	0.19	0.12	0.02	16.27	0.76	21.20	0.98	0.60	0.04	99.59	
JR31-52-3	7R	10	51.57	0.39	0.19	0.02	5.43	0.26	1.02	0.06	2.41	0.17	0.09	0.02	16.47	0.34	21.88	0.46	0.56	0.05	99.62	
JR31-52-3	8I	9	51.81	0.34	0.18	0.03	5.56	0.10	1.07	0.04	2.65	0.36	0.09	0.02	16.94	1.23	21.14	1.66	0.58	0.05	100.04	
JR31-52-3	9I	11	51.10	0.27	0.20	0.02	5.80	0.11	1.08	0.03	2.57	0.14	0.07	0.03	16.62	0.47	21.25	0.69	0.61	0.02	99.31	
JR31-52-4	4C	11	51.82	0.20	0.21	0.02	5.96	0.25	1.21	0.05	2.23	0.11	0.07	0.02	15.49	0.13	22.28	0.17	0.63	0.04	99.89	
JR31-52-4	4R	11	51.84	0.32	0.23	0.03	5.75	0.52	1.15	0.10	2.32	0.08	0.07	0.01	15.47	0.22	22.55	0.19	0.55	0.04	99.92	
JR31-52-5	1C	10	51.62	1.14	0.17	0.06	6.62	0.28	1.21	0.16	3.15	1.68	0.11	0.03	18.01	6.21	18.67	8.30	0.49	0.22	100.05	

Table 3: Cpx major elements Cont.

Analysis	Grn[a]	Pts	SiO$_2$	±	TiO$_2$	±	Al$_2$O$_3$	±	Cr$_2$O$_3$	±	FeO	±	MnO	±	MgO	±	CaO	±	Na$_2$O	±	Total	Notes[b]
JR31-52-5	1R	10	52.19	0.29	0.21	0.02	5.28	0.54	0.96	0.08	2.19	0.08	0.09	0.02	15.75	0.46	23.15	0.27	0.42	0.07	100.23	
JR31-52-5	3C	9	51.79	0.36	0.19	0.02	5.68	0.22	1.03	0.05	2.28	0.14	0.09	0.01	16.33	0.62	22.06	0.60	0.55	0.06	100.00	
JR31-52-5	5I	11	51.78	0.34	0.18	0.02	5.98	0.18	1.04	0.04	2.64	0.26	0.04	0.02	16.31	1.07	21.46	1.25	0.56	0.04	99.99	
JR31-52-5	6I	8	51.57	0.37	0.22	0.03	5.96	0.09	1.09	0.03	2.51	0.06	0.04	0.03	15.86	0.22	22.06	0.35	0.56	0.04	99.86	
JR31-52-8	1C	10	51.18	0.28	0.18	0.02	6.21	0.11	1.22	0.05	2.77	0.38	0.12	0.02	16.38	1.37	20.87	1.92	0.56	0.08	99.49	
JR31-52-8	1R	20	51.55	0.45	0.21	0.03	6.06	0.38	1.16	0.10	2.60	0.45	0.10	0.02	16.39	1.09	21.21	1.71	0.57	0.07	99.85	
JR31-52-8	3I	9	51.71	0.15	0.18	0.01	5.64	0.10	1.11	0.04	2.62	0.27	0.08	0.02	16.17	0.98	21.21	1.35	0.66	0.07	99.38	
JR31-52-8	4R	9	51.91	0.25	0.22	0.02	5.43	0.28	1.01	0.10	2.46	0.08	0.09	0.02	16.19	0.35	21.80	0.40	0.62	0.06	99.74	
RC27-9-6-5	1C	8	51.00	1.13	0.16	0.08	6.75	0.16	1.08	0.16	3.96	1.95	0.12	0.03	19.09	6.28	16.99	8.82	0.46	0.17	99.60	Enr
RC27-9-6-5	1R	5	51.27	0.81	0.27	0.08	4.38	1.76	1.16	0.02	2.66	0.35	0.10	0.03	16.35	0.83	22.65	1.35	0.44	0.08	99.28	Enr
RC27-9-6-5	2C	8	51.26	1.08	0.17	0.07	6.67	0.19	1.14	0.13	3.71	1.63	0.11	0.04	18.34	5.21	18.74	7.56	0.36	0.15	100.51	Trans
RC27-9-6-5	2R	9	51.44	0.71	0.49	0.13	5.65	0.35	1.09	0.04	3.14	0.36	0.09	0.02	17.15	1.22	21.39	1.54	0.42	0.06	100.86	Trans
RC27-9-6-5	3I	6	52.40	0.80	0.49	0.19	2.50	0.80	0.96	0.33	2.23	0.12	0.08	0.02	17.19	0.60	23.37	0.52	0.45	0.16	99.68	Enr
RC27-9-6-5	4C	13	51.57	0.25	0.31	0.04	5.73	0.11	1.08	0.03	3.04	0.45	0.04	0.02	16.25	1.31	21.76	1.89	0.50	0.05	100.28	Enr
RC27-9-6-5	4R	10	52.24	0.71	0.47	0.05	3.61	0.89	0.98	0.09	2.80	0.29	0.10	0.01	16.41	0.82	22.22	0.87	0.39	0.06	99.23	Enr
RC27-9-6-5	5C	8	51.76	1.33	0.34	0.11	5.79	0.57	1.07	0.15	3.91	1.75	0.11	0.04	19.36	5.68	17.42	7.94	0.60	0.27	100.35	Enr
RC27-9-6-5	5R	11	52.45	1.08	0.55	0.15	3.87	0.84	1.19	0.20	2.58	0.49	0.04	0.03	17.39	2.14	21.28	2.57	0.71	0.25	100.06	Enr
RC27-9-6-5	L11C	10	51.3	0.6	0.24	0.03	6.23	1.06	1.13	0.08	3.11	0.29	0.09	0.02	16.30	0.87	22.06	1.67	0.39	0.23	100.85	
RC27-9-6-5	L11R	10	51.8	0.6	0.25	0.03	5.55	0.89	0.88	0.08	2.82	0.44	0.07	0.02	16.46	1.10	22.64	1.73	0.35	0.10	100.82	
RC27-9-6-7	1C	10	51.59	1.43	0.16	0.09	6.33	0.27	1.07	0.18	4.21	2.05	0.14	0.02	20.46	7.42	15.56	10.04	0.33	0.23	99.85	
RC27-9-6-7	1R	10	51.34	0.95	0.22	0.05	5.86	0.53	1.02	0.14	3.05	0.93	0.11	0.02	16.88	3.37	21.22	4.40	0.35	0.09	100.05	
RC27-9-6-7	3I	10	51.49	0.38	0.23	0.03	5.76	0.12	0.93	0.06	3.09	0.56	0.08	0.02	17.04	2.04	21.26	2.57	0.39	0.09	100.27	
RC27-9-6-7	5I	7	50.83	0.99	0.25	0.04	5.50	0.93	0.92	0.17	2.78	0.22	0.09	0.02	16.39	0.55	22.59	1.03	0.41	0.09	99.78	

[a] Grain number and core (C), rim (R) or interstitial (I). Interstitial grains are < 1 mm diameter. L preceding a grain number indicates *Lee* (1997) data for dredge RC27-9-6 samples.

[b] Abbreviations: Dep, Trans and Enr refer to depleted, transitional and enriched zones of the cryptically metasomatized samples.

Table 4: Major element compositions of Opx, in wt%.

Analysis	Grn[a]	Pts	SiO$_2$	±	TiO$_2$	±	Al$_2$O$_3$	±	Cr$_2$O$_3$	±	FeO	±	MnO	±	MgO	±	CaO	±	Na$_2$O	±	Total	Notes[b]
6K-458-1	1C	8	53.01	1.81	0.10	0.04	4.17	0.89	1.38	0.81	6.43	1.08	0.21	0.07	32.27	1.15	1.24	1.26	0.07	0.07	98.88	Enr
6K-458-1	1R	8	54.82	0.44	0.09	0.02	5.05	0.14	0.85	0.03	6.05	0.15	0.14	0.01	32.43	0.51	1.29	0.71	0.02	0.02	100.74	Enr
6K-458-3	1C	13	54.17	0.29	0.09	0.03	5.64	0.24	0.75	0.03	6.12	0.23	0.12	0.02	30.56	0.88	1.97	1.04	0.01	0.01	99.42	Dep
6K-458-3	1C	9	54.77	0.24	0.08	0.02	4.91	0.11	0.62	0.02	6.23	0.16	0.12	0.03	31.18	0.46	1.32	0.65	0.00	0.00	99.24	Dep
6K-465-2	1C	10	55.44	0.29	0.09	0.01	4.17	0.16	0.64	0.01	6.32	0.12	0.12	0.01	32.18	0.37	1.58	0.41	0.03	0.01	100.57	Dep
6K-465-2	1R	10	55.78	0.34	0.09	0.01	3.34	0.46	0.61	0.02	6.35	0.10	0.12	0.02	33.04	0.45	1.19	0.20	0.03	0.01	100.54	Dep
6K-465-2	2C	3	53.42	0.30	0.07	0.02	5.51	0.21	0.81	0.05	6.12	0.29	0.13	0.03	31.24	0.53	1.77	0.84	0.00	0.00	99.07	Dep
6K-466-1	1C	10	54.70	0.50	0.08	0.03	4.57	0.15	0.77	0.03	5.80	0.29	0.14	0.05	31.80	0.91	2.37	1.22	0.04	0.04	100.27	
6K-466-1	1R	10	55.77	0.30	0.07	0.01	3.98	0.07	0.60	0.03	5.92	0.15	0.14	0.02	32.74	0.36	1.36	0.45	0.02	0.02	100.59	
6K-466-1	2I	6	54.89	0.33	0.07	0.01	3.49	0.14	0.44	0.02	5.96	0.13	0.17	0.02	34.22	0.30	0.78	0.06			100.01	
6K-643-13	1C	10	54.19	0.21	0.05	0.01	5.07	0.10	0.90	0.04	5.97	0.16	0.13	0.02	31.15	0.56	2.18	0.55	0.02	0.01	99.65	
6K-643-13	1R	9	54.90	0.46	0.05	0.02	3.98	0.27	0.67	0.05	6.01	0.30	0.13	0.02	32.05	1.29	1.92	1.75	0.01	0.01	99.71	
JR31-52-3	1C	13	54.36	0.29	0.06	0.02	5.45	0.13	0.90	0.03	5.97	0.17	0.13	0.02	30.94	0.47	1.96	0.56	0.06	0.03	99.84	
JR31-52-3	1R	10	55.17	0.36	0.05	0.01	4.29	0.29	0.58	0.07	6.01	0.19	0.13	0.02	32.00	0.39	1.21	0.40	0.02	0.01	99.45	
JR31-52-4	1C	16	54.25	0.25	0.08	0.02	5.25	0.09	0.71	0.08	5.97	0.20	0.12	0.03	31.24	0.62	1.80	0.79	0.06	0.03	99.47	
JR31-52-4	1R	11	54.46	0.12	0.08	0.01	5.18	0.07	0.79	0.02	5.91	0.23	0.12	0.02	31.07	0.96	2.12	1.28	0.06	0.04	99.80	
JR31-52-4	2I	12	55.77	0.28	0.08	0.01	3.63	0.20	0.43	0.05	6.12	0.11	0.13	0.02	32.81	0.19	0.89	0.08	0.02	0.01	99.89	
JR31-52-5	1C	13	54.17	0.49	0.08	0.01	5.38	0.15	0.81	0.04	5.84	0.16	0.14	0.03	30.86	0.68	2.30	0.89	0.05	0.03	99.63	
JR31-52-5	1R	11	54.59	0.40	0.05	0.02	5.15	0.28	0.76	0.04	5.93	0.18	0.08	0.02	31.78	0.42	1.20	0.37	0.04	0.01	99.58	
JR31-52-8	1C	15	54.45	0.42	0.09	0.02	5.16	0.24	0.80	0.05	5.93	0.18	0.11	0.03	30.88	0.72	2.30	1.00	0.06	0.03	99.79	
JR31-52-8	1R	15	55.82	0.51	0.08	0.01	3.68	0.31	0.42	0.09	6.16	0.16	0.12	0.02	32.64	0.34	0.83	0.26	0.02	0.02	99.76	
JR31-52-8	3I	10	56.00	0.20	0.05	0.01	3.94	0.11	0.57	0.02	6.10	0.10	0.12	0.02	32.37	0.19	1.32	0.17	0.05	0.01	100.53	
RC27-9-6-5	1C	9	55.02	0.52	0.09	0.02	3.82	0.55	0.68	0.04	6.30	0.14	0.09	0.02	31.30	0.60	1.56	0.71	0.04	0.03	98.91	Trans
RC27-9-6-5	1R	10	56.31	0.45	0.13	0.02	2.40	0.19	0.61	0.03	6.54	0.15	0.10	0.02	32.63	0.36	0.88	0.36	0.06	0.08	99.66	Trans
RC27-9-6-5	5I	7	55.77	0.83	0.08	0.01	3.30	0.32	0.70	0.04	6.49	0.02	0.14	0.02	32.39	0.24	1.10	0.31	0.01	0.01	99.99	Enr
RC27-9-6-5	L1C	10	53.9	0.3	0.09	0.03	5.71	0.13	0.76	0.04	6.59	0.50	0.11	0.02	31.11	1.5	2.29	2.1	0.02	0.02	100.58	
RC27-9-6-7	1C	10	54.16	0.27	0.08	0.02	5.25	0.40	0.72	0.04	6.16	0.16	0.14	0.02	31.13	0.65	1.86	0.58	0.01	0.02	99.53	
RC27-9-6-7	1R	10	55.13	0.27	0.06	0.01	4.22	0.15	0.38	0.02	6.46	0.12	0.14	0.02	32.88	0.27	0.59	0.11	0.00	0.01	99.84	

[a] Grain number and core (C), rim (R) or interstitial (I). Interstitial grains are < 1 mm diameter. L preceding a grain number indicates *Lee* (1997) data for dredge RC27-9-6 samples.
[b] Abbreviations: Dep, Trans and Enr refer to depleted, transitional and enriched zones of the cryptically metasomatized samples.

Table 5: Major element compositions of olivines, in wt%.

Sample	Grn[a]	Pts	SiO$_2$	±	FeO	±	MnO	±	MgO	±	NiO	±	Total	Mg#	Notes[b]
6K-458-1	1	6	40.55	0.26	9.22	0.18	0.08	0.03	49.64	0.29	0.34	0.04	99.87	90.6	Enr
6K-465-2	1	6	40.53	0.28	9.63	0.11	0.14	0.02	50.00	0.36	0.32	0.03	100.68	90.3	Dep
6K-465-2	2	6	41.91	0.28	9.39	0.09			49.32	0.19			100.67	90.3	Dep
JR31-52-3	1	7	40.10	0.08	9.45	0.12	0.14	0.02	49.48	0.26	0.40	0.03	99.61	90.3	
JR31-52-5	1	6	40.47	0.12	9.43	0.15	0.16	0.02	49.06	0.09	0.35	0.03	99.51	90.3	
JR31-52-8	1	6	40.22	0.09	9.59	0.24	0.14	0.02	49.04	0.14	0.37	0.02	99.38	90.1	
RC27-9-6-5	L1	6	40.50	0.02	10.32	0.07	0.11	0.01	49.43	0.07	0.35	0.02	100.76	89.5	
RC27-9-6-5	L2	6	40.70	0.30	9.85	0.11	0.11	0.02	49.98	0.31	0.39	0.02	101.12	90.0	
RC27-9-6-5	1	5	40.76	0.17	9.93	0.26	0.13	0.04	49.16	0.31	0.34	0.03	100.36	89.8	Enr
RC27-9-6-7	1	6	41.08	0.18	9.60	0.06	0.14	0.01	49.33	0.61	0.31	0.02	100.50	90.2	

[a] Grain number; L preceding a grain number indicates *Lee* (1997) data for dredge RC27-9-6 samples.

[b] Abbreviations: Dep and Enr refer to depleted and enriched zones of the cryptically metasomatized samples.

Table 6: Major element compositions of spinels, in wt%.

Sample	Grn[a]	Pts	TiO_2	±	Al_2O_3	±	Cr_2O_3	±	Fe_2O_3	±	FeO	±	MnO	±	MgO	±	NiO	±	ZnO	±	Total	Notes[b]
6K-458-1	1	5	0.07	0.06	48.28	1.62	21.93	1.91	0.30	0.27	11.30	0.31	0.12	0.04	18.49	0.33	0.27	0.04	0.00	0.00	100.80	Enr
6K-458-3	1	6	0.05	0.01	55.41	0.41	14.72	0.52	0.00	0.00	11.33	0.15	0.15	0.03	18.90	0.19	0.32	0.02	0.12	0.04	101.06	Dep
6K-465-2	1	6	0.17	0.01	46.54	0.27	20.02	0.22	4.06	0.58	9.34	0.56	0.08	0.02	19.50	0.32	0.27	0.02			99.99	Dep
6K-465-2	2	6	0.29	0.02	28.89	1.05	37.78	0.59	2.55	0.56	16.49	0.49	0.25	0.04	12.89	0.17	0.11	0.03			99.34	Dep
6K-465-2	3	6	0.26	0.03	39.47	1.12	28.23	1.18	1.58	0.33	13.18	0.26	0.17	0.02	16.16	0.26	0.18	0.02			99.25	Dep
6K-466-1	1	6	0.10	0.02	48.21	0.16	19.61	0.16	2.97	0.31	8.47	0.15	0.09	0.02	20.17	0.14	0.29	0.02			99.92	
6K-643-13	1	4	0.02	0.03	47.53	0.31	20.85	0.14	1.18	0.19	10.78	0.14	0.11	0.03	18.36	0.03	0.33	0.01	0.00	0.00	99.17	
JR31-52-3	1	6	0.02	0.02	53.01	0.44	16.48	0.27	0.36	0.31	11.03	0.29	0.15	0.03	19.01	0.13	0.31	0.03			100.37	
JR31-52-4	2	6	0.09	0.11	52.57	0.18	16.07	0.31	0.00	0.00	12.13	0.26	0.12	0.03	18.08	0.14	0.28	0.03			99.37	
JR31-52-5	1	6	0.04	0.01	51.41	1.23	17.53	1.09	0.86	0.50	10.90	0.39	0.13	0.01	18.90	0.25	0.30	0.03			100.09	
JR31-52-8	1	6	0.07	0.02	52.46	0.17	16.73	0.18	0.19	0.20	11.07	0.36	0.11	0.03	18.86	0.15	0.31	0.03			99.81	
RC27-9-6-5	1	6	0.21	0.03	42.99	3.91	24.44	3.71	2.07	0.66	13.16	0.96	0.17	0.05	16.57	0.96	0.30	0.03	0.18	0.07	100.12	Dep
RC27-9-6-5	2	6	0.17	0.03	27.59	1.14	39.19	0.61	2.71	0.39	17.01	0.30	0.23	0.03	12.43	0.28	0.19	0.03	0.05	0.10	99.66	Dep
RC27-9-6-5	L1	6	0.32	0.09	46.56	2.30	20.61	2.26	2.43		11.63	0.60	0.25	0.02	17.87	0.44	0.41	0.03			100.14	
RC27-9-6-7	1	3	0.00	0.01	49.49	2.90	15.73	0.46	3.74	2.34	11.29	1.03	0.24	0.26	18.12	1.03	0.33	0.03	0.00	0.00	99.03	
RC27-9-6-7	2	6	0.00	0.00	51.79	0.76	15.58	0.57	1.67	0.44	11.95	0.31	0.07	0.03	18.15	0.38	0.31	0.02	0.00	0.00	99.57	

[a] Grain number; L preceding a grain number indicates *Lee* (1997) data for dredge RC27-9-6 samples.
[b] Abbreviations: Dep and Enr refer to depleted and enriched zones of the cryptically metasomatized samples.

Table 7: Major element compositions of plagioclase, in wt%.

Analysis	Grn[a]	Pts	SiO$_2$	±	Al$_2$O$_3$	±	FeO	±	CaO	±	Na$_2$O	±	Total	An
6K-465-2	1	6	45.34	0.32	35.20	0.38	0.11	0.02	18.00	0.35	1.02	0.19	99.72	90.7
6K-465-2	2	6	44.75	0.14	35.35	0.15	0.13	0.04	18.42	0.11	0.74	0.04	99.44	93.2
6K-465-2	3	7	45.29	0.36	35.02	0.35	0.15	0.04	18.04	0.21	1.06	0.07	99.60	90.4
RC27-9-6-5	L1	6	47.2	0.4	33.62	0.28	0.10	0.03	17.02	0.18	1.84	0.19	101.03	83.6
RC27-9-6-5	1	6	47.19	0.32	34.64	0.40	0.11	0.04	16.75	0.30	1.74	0.21	100.44	84.1

[a] All grains are interstitial and from the depleted zones of cryptically metasomatized peridotites. L preceding a grain number indicates *Lee* (1997) data for dredge RC27-9-6 samples.

Table 8: Ion probe trace element concentrations in ppm for cryptically metasomatized peridotite Cpx.

Sample	Grain	Type[a]	La	Ce	Nd	Sm	Eu	Dy	Er	Yb	Na$_2$O	Ti	Cr	Sr	Y	Zr	Notes[b]
KH1[c]	Cpx		1.220	5.39	5.56	2.12	0.75	2.30	1.12	0.99							
KL2G[d]	Basalt										2.27	15200	290	362.00	27	160.00	
KLB1, Ave, n=21	Cpx		0.223	1.86	3.29	1.70	0.70	2.83	1.67	1.49							
KLB1, Std Dev	Cpx		0.038	0.21	0.38	0.25	0.07	0.25	0.18	0.18							
KLB1, Error (%)	Cpx		17	11	11	15	10	8.9	11	12							
Count Error (%)[e]	Cpx		21	13	10	10	8.2	4.9	6.2	5.5	0.3	0.6	0.2	5.9	2.2	7.0	
Duplicate Error (%)[f]	Cpx		32	37	16	17	17	15	18	19	7.6	11	6.8	14	9.4	17	
6K-458-1	Cpx1	Core	0.588	1.86	1.51	1.28	0.38	2.18	1.24	1.21	0.56	1470	7430	3.05	18.36	5.39	Enr
6K-458-1	Cpx1	Rim	0.725	3.55	3.35	1.78	0.47	3.83	2.16	1.85	0.48	2122	8246	1.72	22.13	23.22	Enr
6K-458-1	Cpx2	Ints	0.658	3.33	3.22	1.95	0.39	4.10	2.06	1.86	0.44	1979	6520	3.11	21.82	26.93	Enr
6K-458-1	Cpx3	Ints	0.790	3.28	3.01	1.46	0.48	3.09	1.58	1.53	0.57	2274	8182	3.08	27.37	21.43	Enr
6K-458-3	Cpx2	Ints	0.332	0.69	1.41	1.25	0.46	2.82	1.43	1.26	0.40	1908	5112	1.84	19.67	3.90	Trans
6K-458-3	Cpx3	Core	0.088	0.22	1.66	1.72	0.55	3.89	1.35	1.88	0.39	2514	6894	3.81	21.41	4.96	Dep
6K-458-3	Cpx3	Rim	0.053	0.25	1.83	1.25	0.45	3.72	1.56	1.77	0.37	2316	5660	4.76	23.93	5.28	Dep
6K-458-3	Cpx4	Core	0.033	0.15	0.71	0.78	0.31	1.82	1.06	0.96	0.44	1374	6040	3.66	13.97	1.83	Dep
6K-458-3	Cpx4	Rim	0.105	0.28	1.05	0.61	0.33	2.04	1.47	1.16	0.49	1541	5624	2.75	15.64	3.11	Dep
6K-458-3	Cpx5	Ints	0.058	0.10	0.78	0.63	0.27	1.93	1.62	1.09	0.45	1934	5006	4.10	16.11	3.98	Dep
6K-458-3	Cpx6	Ints	0.428	1.60	1.51	1.01	0.35	3.18	2.03	1.88							Trans
6K-465-2	Cpx1	Core1	0.015	0.04	0.47	0.70	0.33	2.60	1.53	1.60	0.33	1312	5485	3.90	15.78	1.83	Dep
6K-465-2	Cpx1	Core2	0.038	0.18	0.67	0.85	0.36	2.68	1.83	1.59							Dep
6K-465-2	Cpx1	Rim1	0.008	0.05	0.71	0.90	0.30	3.31	1.82	1.72	0.31	1858	5802	2.81	20.02	2.69	Dep
6K-465-2	Cpx1	Rim2	0.029	0.04	0.53	0.73	0.21	1.82	1.23	0.89							Dep
6K-465-2	Cpx2	Core1	0.005	0.03	0.37	0.47	0.20	1.64	1.13	1.10	0.22	1003	4291	1.16	6.63	0.80	Dep
6K-465-2	Cpx2	Core2	0.002	0.03	0.31	0.44	0.20	1.29	0.84	0.90	0.28	1169		1.59	12.22	1.66	Dep
6K-465-2	Cpx2	Core3	0.005	0.05	0.40	0.44	0.22	1.44	0.71	0.77	0.27	1183		1.08	11.40	1.30	Dep
6K-465-2	Cpx2	Core4	0.004	0.03	0.32	0.57	0.22	1.51	0.83	1.00							Dep
6K-465-2	Cpx2	Core5	0.011	0.02	0.30	0.49	0.27	1.77	1.09	1.07							Dep
6K-465-2	Cpx2	Rim	0.004	0.04	0.47	0.65	0.17	2.16	1.17	1.26	0.26	1584		6.17	16.97	2.19	Dep
6K-465-2	Cpx3	Core	0.017	0.04	0.41	0.48	0.24	1.97	1.01	1.19	0.22	1073	4669	1.32	10.13	1.33	Dep
6K-465-2	Cpx3	Rim	0.016	0.04	0.50	0.75	0.26	2.64	1.60	1.57	0.24	1774	4506	1.33	14.95	1.61	Dep
6K-465-2	Cpx4	Core	0.007	0.03	0.40	0.56	0.29	2.54	1.63	1.73	0.29	1681	6007	1.47	23.18	2.93	Dep
6K-465-2	Cpx4	Rim	0.012	0.05	0.45	0.41	0.16	1.68	0.98	1.11	0.30	1825	6264	3.42	21.05	2.88	Dep
6K-465-2	Cpx5	Core1	0.863	3.77	2.48	1.10	0.38	2.69	1.92	1.98	0.52	1437	5768	2.27	27.20	7.13	Enr
6K-465-2	Cpx5	Core2	0.971	4.29	2.86	1.41	0.53	3.59	2.78	2.87	0.36	1283		1.27	22.06	2.92	Enr
6K-465-2	Cpx5	Rim	0.470	2.09	1.82	1.27	0.38	3.17	2.65	2.42	0.17	1877		1.17	38.52	11.86	Enr
6K-465-2	Cpx6	Core1	0.120	0.32	0.47	0.50	0.22	1.63	1.08	0.97	0.29	1069		1.02	13.14	1.19	Trans
6K-465-2	Cpx6	Mdpt2	0.048	0.14	0.45	0.52	0.26	1.69	1.02	1.09	0.37	1143		1.28	13.21	1.21	Trans
6K-465-2	Cpx6	Mdpt3	0.159	0.62	0.73	0.69	0.26	2.34	1.53	1.83	0.37	1442	5376	3.21	22.45	3.49	Trans
6K-465-2	Cpx6	Mdpt4	0.064	0.11	0.35	0.56	0.26	1.64	1.02	0.86	0.30	1001		0.98	11.30	1.12	Trans
6K-465-2	Cpx6	Mdpt5	0.099	0.23	0.47	0.52	0.28	1.54	1.09	0.91	0.30	1053		1.01	13.07	1.27	Trans
6K-465-2	Cpx6	Mdpt6	0.182	0.71	0.67	0.64	0.25	1.83	1.34	1.42	0.29	1108		1.13	14.55	1.45	Trans
6K-465-2	Cpx6	Mdpt7	0.383	1.34	1.14	0.72	0.25	2.39	1.63	2.24	0.41	1426	5305	1.72	26.16	3.58	Trans
6K-465-2	Cpx6	Rim8	0.377	1.73	2.17	1.10	0.32	2.71	1.77	1.97	0.27	1233		0.93	21.25	4.69	Trans

Sample	Grain	Type[a]	La	Ce	Nd	Sm	Eu	Dy	Er	Yb	Na$_2$O	Ti	Cr	Sr	Y	Zr	Notes[b]
6K-465-2	Cpx6	Rim9	0.412	2.05	1.77	0.99	0.30	3.12	2.21	2.78	0.48	1774	6731	3.06	30.18	7.65	Trans
6K-465-2	Cpx7	Core	0.169	0.60	0.81	0.73	0.35	2.40	1.93	1.70							Enr
6K-465-2	Cpx7	Rim	0.164	0.65	0.77	0.48	0.29	2.06	1.55	1.40							Enr
6K-465-2	Cpx8	Core1	0.021	0.08	0.50	0.69	0.33	2.05	1.28	1.19	0.43	1222		0.92	14.25	1.24	Dep
6K-465-2	Cpx8	Core2	0.021	0.06	0.48	0.52	0.18	1.30	0.92	0.64	0.42	1186		1.26	13.19	1.37	Dep
6K-465-2	Cpx8	Core3	0.021	0.06	0.39	0.49	0.26	1.48	1.02	0.92							Dep
6K-465-2	Cpx8	Rim1	0.071	0.22	0.44	0.45	0.20	1.50	1.10	0.87							Dep
6K-465-2	Cpx8	Rim2	0.068	0.33	0.75	0.58	0.28	2.23	1.70	1.29	0.38	1528		0.83	18.63	1.76	Dep
6K-465-2	Cpx8	Rim3	0.089	0.34	0.76	0.72	0.30	2.41	1.71	1.67	0.40	1597		0.80	18.87	1.75	Dep
6K-465-2	Cpx9	Rim1	0.601	2.98	2.72	1.24	0.28	3.15	2.11	1.95	0.40	1396	5186	2.69	28.75	10.15	Enr
6K-465-2	Cpx9	Rim2	0.941	5.33	4.84	2.23	0.51	5.31	4.17	3.76	0.33	1398		1.03	31.12	9.39	Enr
6K-465-2	Cpx9	Rim3	1.344	7.99	7.57	3.83	0.79	7.78	5.58	5.46	0.37	2075		1.41	42.81	16.63	Enr
6K-465-2	Cpx10	Ints	0.009	0.04	0.49	0.78	0.24	3.08	1.82	1.50	0.34	1705	4662	3.45	9.89	1.32	Dep
6K-465-2	Cpx11	Core1	0.007	0.06	0.54	0.81	0.29	2.05	1.31	1.35							Dep
6K-465-2	Cpx11	Core2	0.007	0.05	0.50	0.66	0.23	2.21	1.31	1.24							Dep
6K-465-2	Cpx11	Rim	0.005	0.05	0.44	0.57	0.19	1.95	1.16	1.12							Dep
6K-465-2	Cpx12	Ints	0.010	0.04	0.42	0.52	0.23	1.94	1.24	1.29							Dep
RC27-9-6-5	Cpx1	Core1	0.861	2.77	1.54	0.64	0.36	1.77	1.17	1.23	0.29	1273	5768	1.63	18.74	4.23	Enr
RC27-9-6-5	Cpx1	Core2	0.858	2.29	1.45	0.66	0.36	2.04	0.98	1.36	0.48	1194	6389	2.26	14.35	1.05	Enr
RC27-9-6-5	Cpx1	Rim	1.124	6.93	9.11	4.01	0.98	5.65	2.75	2.00	0.24	3659	4979	3.15	42.21	82.90	Enr
RC27-9-6-5	Cpx2	Core1	0.021	0.05	0.25	0.30	0.16	1.12	0.64	0.73	0.36	1007	5579	0.83	11.61	1.08	Trans
RC27-9-6-5	Cpx2	Mdpt2									0.30	1070	6809	1.73	13.86	1.14	Trans
RC27-9-6-5	Cpx2	Mdpt3	0.060	0.13	0.20	0.36	0.17	1.43	0.84	0.76	0.39	1121	5698	1.28	13.07	1.17	Trans
RC27-9-6-5	Cpx2	Mdpt4	0.194	0.37	0.42	0.38	0.18	1.66	0.88	0.90	0.36	1270	7237	1.91	16.11	1.30	Trans
RC27-9-6-5	Cpx2	Mdpt5	0.879	3.74	2.35	1.27	0.45	2.59	1.67	1.63	0.39	1544	6811	2.40	26.81	13.06	Trans
RC27-9-6-5	Cpx2	Mdpt6	0.999	4.40	3.51	1.35	0.48	3.06	1.76	1.66	0.41	1873	6857	2.16	29.80	18.35	Trans
RC27-9-6-5	Cpx2	Rim7	1.001	5.21	5.37	2.20	0.62	4.57	2.32	1.98	0.31	2792	4956	1.92	31.24	45.18	Trans
RC27-9-6-5	Cpx3	Ints	1.004	7.00	9.36	4.96	0.99	6.44	2.78	2.43	1.19	7912	6282	9.01	58.17	150.43	Enr
RC27-9-6-5	Cpx4	Core	1.311	6.33	4.68	1.74	0.62	3.24	1.56	1.51	0.55	1471	5683	2.26	23.67	16.90	Enr
RC27-9-6-5	Cpx4	Rim	1.001	4.58	5.23	1.97	0.61	3.69	1.83	1.53	0.35	2646	5562	2.97	30.66	51.25	Enr
RC27-9-6-5	Cpx5	Core	1.446	6.11	3.30	0.96	0.51	2.35	1.41	1.49	0.77	1632	6555	3.24	25.19	21.34	Enr
RC27-9-6-5	Cpx5	Rim	1.141	5.69	5.93	2.65	0.65	4.16	2.32	2.12	0.50	2776	8399	2.38	37.76	53.11	Enr

[a] Ints refers to interstitial grain, <1 mm diameter. Numbered analyses and Mdpt (midpoint between core and rim) refer to multiple analyses of grains in cryptically metasomatized samples.

[b] Abbreviations for lithologies (blank indicates residual peridotite): Dep, Trans and Enr are depleted, transitional and enriched zones in cryptically metasomatized samples.

[c] Cpx from Kilbourne Hole (*Irving and Frey*, 1984), used as a standard for REEs.

[d] Kilauea tholeiitic basalt glass (*Jochum et al.*, 2000), used as a standard for the other trace elements.

[e] Percent error based on average counting error among Cpx analyses, including unpublished analyses.

[f] Percent error based on average difference among duplicate Cpx analyses, including unpublished duplicate pairs.

Table 9: Ion probe trace element concentrations in ppm for residual abyssal peridotite Cpx.

Sample	Grain[a]	Type[b]	La	Ce	Nd	Sm	Eu	Dy	Er	Yb	Na₂O	Ti	Cr	Sr	Y	Zr
6K-466-1	Cpx1	Core	0.011	0.06	0.41	0.49	0.20	1.57	0.70	0.91	0.46	1294	9529	1.22	10.77	2.31
6K-466-1	Cpx1	Rim	0.005	0.05	0.52	0.39	0.17	1.75	0.89	0.75	0.41	1400	8847	1.61	12.37	2.53
6K-466-1	Cpx3	Ints	0.064	0.07	0.47	0.38	0.20	1.50	0.85	0.79	0.40	1480	8195	1.77	11.77	2.89
6K-466-1	Cpx3D	Ints									0.39	1628	8259	2.38	12.75	3.59
6K-643-1	Cpx1	Ints	0.024	0.04	0.23	0.29	0.15	1.74	0.93	1.30	0.20	913	6261	1.15	9.90	0.94
6K-643-1	Cpx1D	Ints	0.016	0.02	0.25	0.32	0.26	2.36	1.26	1.60	0.18	1032	6518	1.41	10.39	0.90
6K-643-1	Cpx2	Core	0.018	0.04	0.26	0.25	0.18	1.37	0.94	0.85	0.21	579	5425	1.27	5.30	0.66
6K-643-1	Cpx2	Rim	0.023	0.04	0.20	0.25	0.12	0.83	0.61	0.54	0.34	918	5538	1.39	8.98	1.00
6K-643-1	Cpx4	Core	0.025	0.04	0.25	0.33	0.15	0.92	0.65	0.65	0.42	809	5284	1.33	9.26	1.87
6K-643-1	Cpx4	Rim	0.023	0.04	0.39	0.39	0.19	1.35	0.95	0.81	0.35	714	4664	1.63	7.01	1.31
6K-643-1	Cpx8	Symp	0.019	0.06	0.31	0.45	0.16	1.34	0.71	0.80	0.29	905	5245	1.41	8.71	1.71
6K-643-1	Cpx8D	Symp	0.017	0.06	0.28	0.54	0.17	1.49	0.83	0.92	0.31	1261	4916	1.78	12.00	1.12
6K-643-6	Cpx5	Ints	0.027	0.05	0.20	0.25	0.13	0.86	0.54	0.51	0.44	1233	9453	2.39	8.26	1.69
6K-643-6	Cpx6	Ints	0.020	0.05	0.15	0.32	0.12	0.92	0.58	0.55	0.48	1223	10072	1.81	8.37	6.04
6K-643-13	Cpx1	Ints	0.007	0.01	0.10	0.30	0.10	0.97	0.71	0.63	0.30	961	5195	1.90	9.95	0.73
6K-643-13	Cpx2	Core	0.021	0.02	0.17	0.31	0.23	1.42	0.82	0.88	0.13	602	5945	1.25	5.23	0.66
6K-643-13	Cpx2	Rim		0.02	0.09	0.28	0.09	1.33	0.89	0.75	0.24	877	6416	1.60	9.60	0.73
6K-643-13	Cpx3	Ints	0.004	0.03	0.11	0.15	0.08	0.87	0.63	0.46	0.28	1047	3633	1.68	8.53	0.76
6K-649-5	Cpx1	Core	0.005	0.00	0.22	0.26	0.13	1.13	0.85	0.96	0.26	683	6554	2.20	9.12	0.65
6K-649-5	Cpx1	Rim	0.032	0.02	0.25	0.27	0.17	1.33	0.92	0.91	0.27	802	5774	1.60	9.62	0.95
6K-649-5	Cpx2	Ints	0.025	0.04	0.15	0.23	0.13	1.42	0.66	0.96	0.17	947	11618	1.26	13.05	1.17
6K-649-5	Cpx4	Ints	0.020	0.03	0.23	0.25	0.12	1.28	0.85	1.04						
6K-649-5	Cpx5	Core	0.016	0.02	0.10	0.15	0.09	1.17	0.67	0.95						
6K-649-5	Cpx5	Rim	0.016	0.02	0.22	0.17	0.13	1.40	0.77	1.06						
6K-649-5	Cpx6	Ints	0.012	0.02	0.16	0.12	0.07	0.94	0.53	1.04	0.30	756	4771	1.28	8.10	1.17
6K-649-5	Cpx7	Ints	0.015	0.01	0.11	0.08	0.06	0.87	0.49	0.76						
6K-649-5	Cpx8	Ints	0.007	0.02	0.18	0.24	0.08	1.32	0.84	1.01						
6K-649-5	Cpx9	Ints	0.021	0.02	0.17	0.15	0.11	1.35	0.71	1.01	0.33	748	4813	3.71	8.20	2.24
JR31-52-3	Cpx4	Core	0.007	0.03	0.27	0.38	0.19	1.36	0.77	0.78	0.53	912	10956	0.96	11.03	0.87
JR31-52-3	Cpx4	Rim	0.009	0.06	0.26	0.43	0.17	1.61	0.77	0.79	0.51	941	10004	0.86	11.15	0.91
JR31-52-3	Cpx5	Core	0.012	0.03	0.22	0.34	0.13	1.09	0.62	0.63						
JR31-52-3	Cpx5	Rim	0.015	0.03	0.26	0.31	0.18	1.01	0.63	0.62						
JR31-52-3	Cpx5D	Rim	0.011	0.05	0.29	0.39	0.17	1.18	0.65	0.63						
JR31-52-3	Cpx6	Ints	0.008	0.05	0.30	0.31	0.17	1.15	0.64	0.61						
JR31-52-3	Cpx7	Core	0.005	0.03	0.35	0.47	0.16	1.19	0.74	0.71	0.50	904	10097	0.93	10.13	0.90
JR31-52-3	Cpx7	Rim	0.030	0.04	0.34	0.36	0.20	1.41	0.83	0.84	0.49	1071	8866	1.15	10.40	0.96
JR31-52-3	Cpx9	Ints	0.001	0.03	0.26	0.30	0.19	1.43	0.80	0.81	0.48	1018	8834	1.35	10.20	0.82
JR31-52-4	Cpx3	Core	0.001	0.01	0.16	0.21	0.06	0.65	0.38	0.32						
JR31-52-4	Cpx3	Rim	0.002	0.03	0.31	0.23	0.10	0.72	0.55	0.52						
JR31-52-4	Cpx4	Core	0.005	0.03	0.33	0.40	0.15	1.34	0.86	0.71	0.39	1052	10374	0.89	12.14	0.81
JR31-52-4	Cpx4	Rim	0.005	0.03	0.34	0.40	0.15	1.38	0.84	0.70	0.30	1426	13683	1.12	16.93	1.26
JR31-52-5	Cpx1	Core	0.005	0.02	0.30	0.49	0.20	1.43	0.77	0.76	0.43	920	10969	0.59	12.06	1.04
JR31-52-5	Cpx1	Rim	0.008	0.01	0.26	0.34	0.22	1.39	0.77	0.82	0.29	1126	7950	0.64	12.58	1.36
JR31-52-5	Cpx3	Core	0.011	0.02	0.28	0.42	0.21	1.52	0.89	0.88	0.35	1126	10428	1.23	14.01	0.88
JR31-52-5	Cpx5	Ints	0.009	0.02	0.21	0.33	0.12	1.00	0.69	0.61	0.39	1002	8800	0.91	11.27	0.85

Table 9: Residual peridotite Cpx trace elements in ppm, cont.

Sample	Grain[a]	Type[b]	La	Ce	Nd	Sm	Eu	Dy	Er	Yb	Na$_2$O	Ti	Cr	Sr	Y	Zr
JR31-52-8	Cpx1	Core	0.008	0.02	0.25	0.27	0.16	1.12	0.64	0.71	0.37	730	10371	0.52	7.62	0.61
JR31-52-8	Cpx1	Rim	0.009	0.04	0.31	0.32	0.18	1.29	0.86	0.70	0.47	1097	9310	0.87	10.98	0.75
JR31-52-8	Cpx1D	Rim	0.006	0.04	0.34	0.41	0.21	1.48	0.77	0.82						
JR31-52-8	Cpx3	Ints	0.013	0.04	0.41	0.44	0.17	1.39	0.79	0.72	0.50	1213	11035	0.99	12.42	0.99
JR31-52-8	Cpx4	Rim	0.006	0.04	0.30	0.40	0.16	1.36	0.83	0.92	0.42	959	5842	2.02	8.68	0.78
JR31-52-8	Cpx5	Ints	0.029	0.07	0.46	0.49	0.23	1.52	0.92	0.85	0.48	1086	10099	0.91	10.48	0.83
RC27-9-6-7	Cpx1	Core	0.011	0.05	0.21	0.49	0.20	1.04	0.52	0.48	0.12	387	4695	1.31	3.37	0.72
RC27-9-6-7	Cpx1	Rim	0.003	0.05	0.52	0.72	0.24	1.59	0.96	0.72	0.31	1235	4952	1.82	12.74	1.52
RC27-9-6-7	Cpx3	Ints	0.008	0.04	0.22	0.52	0.22	1.65	0.73	0.83	0.29	1196	4220	1.39	11.13	1.26
RC27-9-6-7	Cpx5	Ints	0.014	0.04	0.44	0.73	0.32	2.18	1.06	0.87	0.43	1515	4490	1.63	12.59	1.70

[a] D following a grain number indicates duplicate analysis.

[b] Ints refers to interstitial grain, <1 mm diameter; Symp refers to symplectite of Cpx with Sp $\pm$ Opx; Numbered analyses and Mdpt (midpoint between core and rim) refer to multiple analyses of grains in cryptically metasomatized samples.

Table 10: Ion probe trace element concentrations in ppm for cryptically metasomatized peridotite Plag.

Sample	Grain[a]	La	Ce	Nd	Sm	Eu	Dy	Er	Yb	Na_2O	Ti	Cr	Sr	Y	Zr
Count Error (%)[b]	Plag	8	5	10	23	7	28	22	31	0	3	12	3	14	21
6K-465-2	Plag1									1.33			57.8	0.95	
6K-465-2	Plag2									0.24			38.6	0.35	
6K-465-2	Plag3									0.94	52		2.5	0.33	0.41
6K-465-2	Plag4									1.02	52		1.4	0.18	0.33
6K-465-2	Plag5									1.02	60		31.8	0.29	0.37
6K-465-2	Plag6									0.96	52		1.3	0.34	0.46
RC27-9-6-5	Plag1	1.23	1.73	0.27	0.02	0.23	0.01	0.08	0.02	1.59	36	2.58	6.5	0.06	0.12

[a] All grains are interstitial and from the depleted zones of cryptically metasomatized peridotites.

[b] Percent error based on average counting error among plagioclase analyses, including unpublished analyses.

59

Table 11: Calculated timescales for mantle upwelling and diffusive equilibration

T (°C)	α_T[a]	z (km)	t_U[b] (My)	P (Pa)	D_{Ce}[c] (m^2/s)	t_{eq} Ce[d] r=1 mm	t_{eq} Ce[e] r=1 cm	D_{Yb}[c] (m^2/s)	t_{eq} Yb[d] r=1 mm	t_{eq} Yb[e] r=1 cm	D_{Sr}[f] (m^2/s)	t_{eq} Sr[d] r=1 mm	t_{eq} Sr[e] r=1 cm
1350	10	36	7	1.E+09	4.E-20	0.8 My	80 My	6.E-19	0.05 My	5 My			
1200	5	18	3	6.E+08	2.E-21	20 My	2 Gy	4.E-20	0.8 My	80 My	3.8E-13	.08 Yr	8 Yr
1100	3.8	14	2	5.E+08	1.E-22	300 My	30 Gy	4.E-21	9 My	900 My	8.7E-17	400 Yr	.04 My
1000	3.1	11	2	4.E+08	5.E-24	6 Gy	600 Gy	2.E-22	140 My	14 Gy	9.5E-19	30 Ky	3 My
700	1.7	6	1	2.E+08	8.E-30	4.E+15 Yr	4.E+17 Yr	2.E-27	2.E+13 Yr	2.E+15 Yr	1.5E-24	20 Gy	2000 Gy

[a] Scaling factor to calculate the depth to a given isotherm using the equation $L_T^* = \alpha_T \kappa / v_H$, where κ is the thermal diffusivity, $10^{-6} m^2/s$, and v_H is the ridge half spreading rate of 8.7 mm/yr from *Baines et al.* (2007). Scaling relation is based on the finite element model for ridge thermal structure from *Montési and Behn* (2007).

[b] Upwelling time from a given isotherm to the seafloor, derived from the scaling relation for depth and the upwelling velocity during ridge corner flow, $v_U = \frac{2}{\pi} v_H$ (*Batchelor*, 1967).

[c] Diffusion coefficients from *Van Orman et al.* (2001).

[d] Equilibration time for a grain of 1 mm radius.

[e] Equilibration time for a grain of 1 cm radius.

[f] Diffusion coefficients from *Sneeringer et al.* (1984).